processes

MDPI

Article

Flow Visualisation and Evaluation Studies on Metalworking Fluid Applications in Manufacturing Processes—Methods and Results

Udo Fritsching [1,2,3,*], Lizoel Buss [2], Teresa Tonn [2], Lukas Schumski [1], Jurgen Gakovi [1], Johnson David Hatscher [1], Jens Sölter [1,2,3], Kerstin Avila [2,4], Bernhard Karpuschewski [1,2,3], Julian Frederic Gerken [5], Tobias Wolf [5], Dirk Biermann [5], Christian Menze [6], Hans-Christian Möhring [6], Elio Tchoupe [7], Lukas Heidemanns [7], Tim Herrig [7], Andreas Klink [7], Kaissar Nabbout [8], Martin Sommerfeld [8], Fabian Luther [9], Ingo Schaarschmidt [10], Andreas Schubert [10] and Markus Richter [9]

1 Faculty of Production Engineering, University of Bremen, Bibliothekstr. 1, 28359 Bremen, Germany; schumski@iwt-bremen.de (L.S.); soelter@iwt.uni-bremen.de (J.S.); karpuschewski@iwt-bremen.de (B.K.)
2 Leibniz-Institute for Materials Engineering IWT, Badgasteiner Str. 3, 28359 Bremen, Germany; l.buss@iwt.uni-bremen.de (L.B.); t.tonn@iwt.uni-bremen.de (T.T.); kerstin.avila@uni-oldenburg.de (K.A.)
3 MAPEX Center for Materials and Processes, University of Bremen, 28359 Bremen, Germany
4 Institute of Physics, University of Oldenburg, Küpkersweg 70, 26129 Oldenburg, Germany
5 Institute of Machining Technology, TU Dortmund University, Baroper Str. 303, 44227 Dortmund, Germany; julian.gerken@tu-dortmund.de (J.F.G.); tobias2.wolf@tu-dortmund.de (T.W.); dirk.biermann@tu-dortmund.de (D.B.)
6 Institute for Machine Tools—IfW, University of Stuttgart, Holzgartenstraße 17, 70174 Stuttgart, Germany; christian.menze@ifw.uni-stuttgart.de (C.M.); hc.moehring@ifw.uni-stuttgart.de (H.-C.M.)
7 Laboratory for Machine Tools and Production Engineering (WZL), RWTH Aachen University, Campus-Boulevard 30, 52074 Aachen, Germany; e.tchoupe_sambou@wzl.rwth-aachen.de (E.T.); l.heidemanns@wzl.rwth-aachen.de (L.H.); t.herrig@wzl.rwth-aachen.de (T.H.); a.klink@wzl.rwth-aachen.de (A.K.)
8 Multiphase Flow Systems, Institute for Process Engineering, Otto-von-Guericke-University Magdeburg, Hoher Weg 7b, 06120 Halle an der Saale, Germany; kaissar.deoliveira@ovgu.de (K.N.); martin.sommerfeld@ovgu.de (M.S.)
9 Applied Thermodynamics, Chemnitz University of Technology, 09107 Chemnitz, Germany; fabian.luther@mb.tu-chemnitz.de (F.L.); m.richter@mb.tu-chemnitz.de (M.R.)
10 Micromanufacturing Technology, Chemnitz University of Technology, 09107 Chemnitz, Germany; ingo.schaarschmidt@mb.tu-chemnitz.de (I.S.); andreas.schubert@mb.tu-chemnitz.de (A.S.)
* Correspondence: ufri@iwt.uni-bremen.de

Abstract: Metalworking operations rely on the successful application of metalworking fluids (MWFs) for effective and efficient operation. Processes such as grinding or drilling often require the use of MWFs for cooling, lubrication, and chip removal. Electrochemical machining processes require electrolyte flow to operate. However, in those machining operations, a fundamental understanding of the mode of action of MWF is lacking due to the unknown flow dynamics and its interaction with the material removal during the process. Important information on the behaviour of MWFs during machining can be obtained from specific experimental flow visualisation studies. In this paper, promising flow visualisation analysis techniques applied to exemplary machining processes (grinding, sawing, drilling, and electrochemical machining) are presented and discussed. Shadowgraph imaging and flow measurements, e.g., particle image velocimetry, allow the identification of typical flow and MWF operating regimes in the different machining processes. Based on the identification of these regimes, efficient machining parameters and MWF applications can be derived. In addition, detailed experimental analyses of MWFs provide essential data for the input and validation of model development and numerical simulations within the Priority Programme SPP 2231 FluSimPro.

Keywords: flow visualisation; manufacturing process; metalworking fluid; high-speed imaging; particle image velocimetry; shadowgraphy

check for updates

Citation: Fritsching, U.; Buss, L.; Tonn, T.; Schumski, L.; Gakovi, J.; Hatscher, J.D.; Sölter, J.; Avila, K.; Karpuschewski, B.; Gerken, J.F.; et al. Flow Visualisation and Evaluation Studies on Metalworking Fluid Applications in Manufacturing Processes—Methods and Results. *Processes* **2023**, *11*, 2690. https://doi.org/10.3390/pr11092690

Academic Editor: Hyun Wook Jung

Received: 27 July 2023
Revised: 17 August 2023
Accepted: 22 August 2023
Published: 7 September 2023

1. Introduction

In the Priority Programme SPP 2231 FluSimPro [1], funded by the German Research Foundation (Deutsche Forschungsgemeinschaft DFG), 24 scientists from 21 research institutions from the fields of production engineering, process engineering, thermal and fluid dynamics, mechanics, and numerical mathematics are working together on the investigation of metalworking fluids (MWFs) in machining processes.

MWFs are used in manufacturing industries in a wide variety of types and formulations, such as mineral or synthetic oils, in pure or diluted form, with or without additives, and new formulations are still being developed [2,3]. MWFs and their specific application in the process have a significant impact on the economic and environmental performance of many manufacturing processes. Key functions of MWFs in manufacturing processes include cooling and lubricating the machining zone while facilitating chip removal [4]. Some recent developments in minimum quantity lubrication (MQL) and the application of MWFs in manufacturing processes are introduced in [5]. As MWFs pose serious environmental problems at the end of their life, strategies have been developed to minimise the use of conventional MWFs or to replace them [6], e.g., dry machining, minimum quantity lubrication (MQL) [7–9], and cryogenic machining [10,11]. For example, in grinding processes, applying the MQL technology can reduce the carbon emissions by 67% and the costs by 92.5% compared to flooded processes [12]. The development of MWF formulations and the modification of application methods or process parameters must be facilitated by a precise knowledge of the process–MWF interaction within the cutting zone, which can be obtained by in situ and model experiments and simulations [13–18].

In terms of content, the question is what role MWFs play in numerous manufacturing processes. Since the effective points of fluids in manufacturing processes are often difficult to access during operation and complex fluid–structure interactions cannot be observed directly, the research programme aims at improved modelling and simulation. With experimentally validated approaches, knowledge-based process optimisations can be realised, for example, concerning the reduction in fluid quantities or targeted feeding.

A powerful tool of MWF flow analysis is used in several approaches within flow visualisation and evaluation studies on metalworking fluid applications in manufacturing processes. This paper describes and discusses the investigations carried out within the overall framework of the SPP 2231 [1], which consists of a total of 12 subprojects numbered from TP01 to TP12. The present paper summarises the results of the seven subprojects (namely TP03, TP04, TP08, TP09, TP10, TP11, and TP12) on the methods and results of MWF flow visualisation within different machining processes (Figure 1).

The machining processes to be presented and discussed in the following subsections are:

- Drilling processes (ejector deep hole drilling, discontinuous drilling, and vibration-assisted drilling);
- Electrochemical machining processes—PECM (with and without magnetic field);
- Sawing process;
- Turning process.

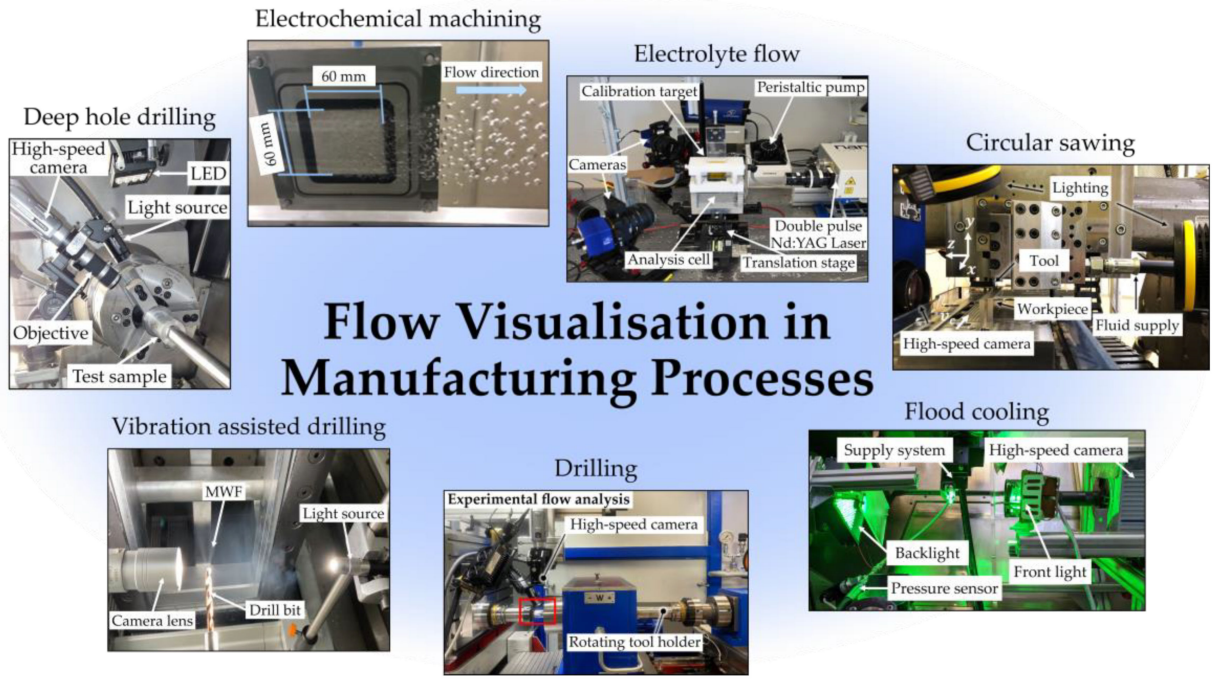

Figure 1. Visualisation of working fluids in metal machining: seven approaches to be detailed in this paper.

2. Manufacturing Processes and Setups for MWF Analyses

2.1. Ejector Deep Hole Drilling (SPP 2231-TP03)

An example of a complex cutting operation that underlines the need for fluid visualisation is ejector deep hole drilling. It is required for a variety of drilling applications with length-to-diameter ratios larger than $l/D > 10$ and high quality demands, e.g., roundness, diameter accuracy, and surface quality. The ejector method makes the advantages of deep hole drilling, such as high material removal rate and high bore quality, usable for the industry in conventional machining centres [19]. In addition to the asymmetrical arrangement of the cutting edges and the use of guide pads on the drilling head, the ejector tool system is characterised by its two concentric tubes and the unique guidance of the MWF. In this system, a partial flow rate Q_1 (operating flow rate) of the total supplied flow rate Q_Σ is directly diverted from the process through openings in the inner pipe, known as ejector nozzles, and used to generate a vacuum inside the inner tube based on the Venturi principle (ejector effect). The remaining portion Q_0 (recirculation flow rate) of the total flow rate Q_Σ enters the cutting zone through the annular chamber between the boring bar and the inner tube. The vacuum created by the ejector effect causes the swarf (coolant–chip mixture) to be sucked in through the chip mouth into the inner pipe. This avoids the need for sealing the machining room, allowing the deep drilling process to be used even without investing in an expensive deep-hole drilling machine [20]. Due to the highly complex MWF flow at the onset of the ejector effect and the lack of process knowledge, this drilling operation offers enormous process optimisation potential and increased efficiency. In order to realise an enhanced fundamental understanding of the ejector effect with its process-typical specialities, an experimental setup combined with a tool system made of polycarbonate glass was developed (Figure 2).

In conventional ejector deep hole drilling, the working and contact zones of the cutting edge and guide pads are not accessible from the outside, so a direct observation of the fluid flow is not possible. In order to observe the MWF supply to the wear elements on the drill head in situ, the opaque drilling wall must be removed. Due to the asymmetrical drill head design, supporting the screwed-on guide pads on the bore wall is necessary, as they guide the tool in the borehole and lead to self-centring. Therefore, removing the bore wall is not

readily possible, and a special test sample had to be developed. To ensure optical access to the material removal zone, it must be assured that the MWF does not obscure the cutting zone. For deep drilling on deep-hole drilling machines, oil is used as the standard MWF. On machining centres, such as the Index G250 (Index-Werke, Esslingen, Germany) used for the experiments, the use of high-additive emulsion (at least 12% oil concentration) is also common. The oil-in-water emulsion Vasco 6000 (Blaser Swisslube, Hasle-Rüegsau, Switzerland) is not transparent. For this reason, conventional water is used as a reference transport medium. Since the existing MWF circuit can only be satisfactorily cleaned with considerable effort, the current machine peripherals are extended with an independent MWF circuit. For MWF supply, an immersion pump (Type STH628A790, Brinkmann, Werdohl, Germany) is adapted to an external intermediate bulk container (IBC). The MWF flows from the ejector system into a collection container. The MWF is pumped back into the IBC via the recirculation pump. The cutting fluid flow in the actual process is measured using high-speed recordings. With the aid of the extended experimental setup with water as the carrier medium for the particles, the opacity was significantly reduced. Consequently, it is possible to capture the particles with a high-speed camera with repeatable accuracy. Due to the ejector effect, air can be temporarily sucked in from the machining room, causing air bubbles to be injected into the flow and causing local opacity. This can be prevented by adjusting the MWF pump volume flow and has to be carried out before the optical measurements are started. The test rig is shown in Figure 3.

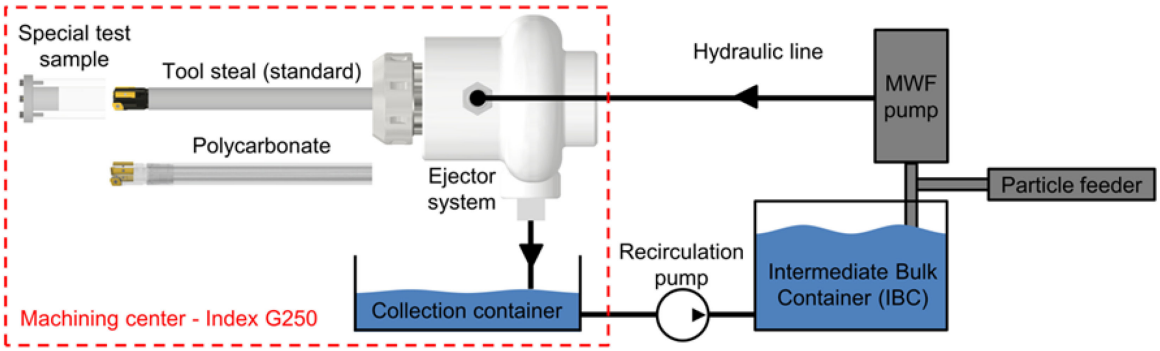

Figure 2. Experimental setup for flow visualisation during ejector deep hole drilling.

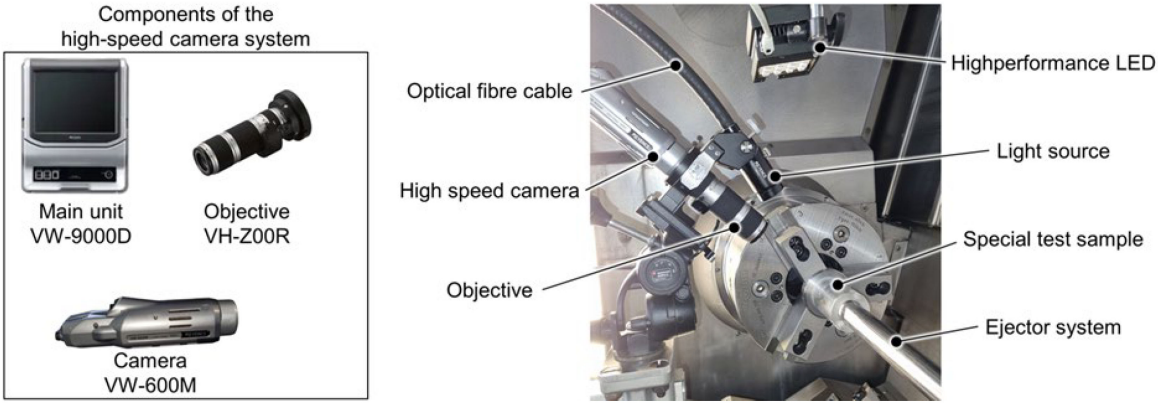

Figure 3. Measurement setup for flow analysis during ejector deep hole drilling.

The modular camera configuration includes a main unit, a high-speed camera, and a close-range objective. The High-Speed Camera VW-9000D (Keyence, Neu-Isenburg, Germany) is used as the main unit. The internal measuring computer processes the memory-intensive recordings and outputs the recorded image material via an integrated LCD monitor. In combination with an adapted high-speed black-and-white camera of type VW-600M (Keyence, Neu-Isenburg, Germany), 4000 images can be captured per

second with an image resolution of 640 × 480 pixels. The frame rate can be increased up to 230,000 frames per second, with a significant reduction in image resolution (160 × 32 pixels). In field tests, 4000 images per second are recorded at a resolution of 640 × 480 pixels. The high-speed camera is equipped with a macro zoom objective of type VH-Z00R (Keyence, Neu-Isenburg, Germany). This objective focuses on a viewing distance of AD = 95 mm and enlarges the recording area by a factor of 5 to 50. The field tests are recorded at 5× magnification. The objective is equipped with a lighting unit of type VW-L1 (Keyence, Neu-Isenburg, Germany). The lighting unit is connected to the main unit via a fibre optic cable. To improve the brightness dynamic, another lighting source of type MultiLed QT (GSVitec, Bad Soden-Salmünster, Germany) is implemented in parallel. It is fixed to the milling spindle of the machining centre using a magnetic stand, and provides 12,000 lumens. To analyse not only the flow in the drill head but also the flow fields inside the double tube system and in the areas of cutting fluid supply to the drill head, a special particle feeder is mounted in front of the MWF pump. In previous test series, analyses were conducted with small particles (diameter d_p = 50 µm). Due to the large bore diameter and the resulting larger analysis area with a greater focal distance, the particles could not be reliably captured with the high-speed camera. The best results with the highest accuracy can be achieved for a particle diameter of d_p = 100 µm. As the particle size is small in relation to the dimensions of the flow channels and tool system, the supplied polyamide particles do not affect the flow inside the tool. A comparison between the fluid flow enriched with polyamide particles and the cutting fluid flow without particles shows identical quantitative flow patterns and characteristics. Additionally, a stable deep drilling process with an ejector effect is possible to achieve with the supplied polyamide particles. To make a quantitative statement about the flow characteristics and velocity, digital analysis methods are used to track the polyamide particles using automated image analysis via the graphical user interface PIVlab—Particle Image Velocimetry of the Matlab software. Compared to manual analysis, this approach offers the further advantage of executing the analysis very efficiently, as the paths of the individual particles do not need to be traced frame by frame, and the distances do not need to be measured. To verify the quantitative flow analysis using PIV, an additional manual analysis was performed for the laminar annular flow, in which three particles were tracked for a defined time step over multiple images, and the distances travelled were measured. A comparison of the automated and manual analysis regarding flow velocities is shown in Figure 4 [21].

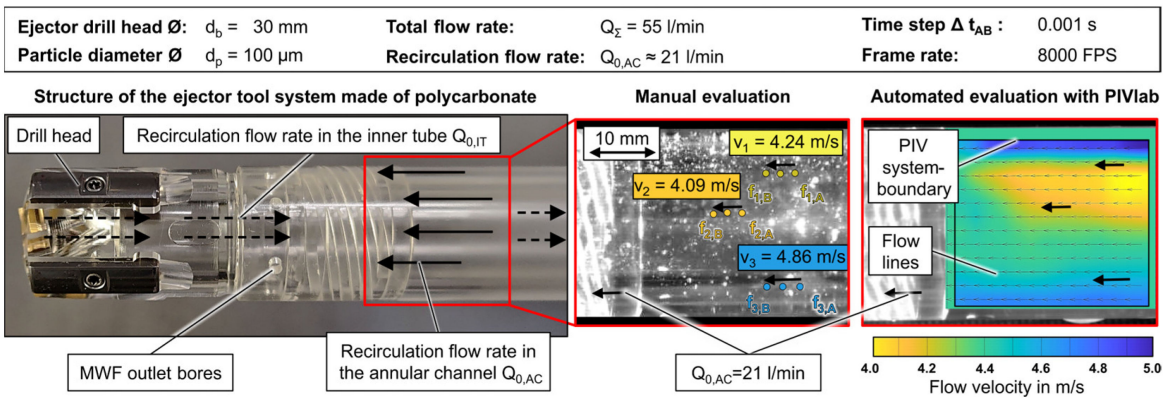

Figure 4. Comparison of manual flow analysis and the automated evaluation with PIVlab.

The evaluated velocity fields show both good qualitative and quantitative agreement with the manually evaluated flow velocities. The evaluations show that PIV is an efficient and valid analysis tool that allows quantitative and qualitative comparisons and assessments of flow characteristics in the tool system in the experimentally recorded MWF flow. In current simulations and experiments, the influence of varying MWF volume flows on flow characteristics and velocity fields is being investigated and analysed using PIV. At the same time, characteristic flow phenomena in the process are evaluated, based on

which flow-optimized drilling head concepts are developed, which allow improved MWF supply to the cutting edges as well as an entry of the ejector effect at lower MWF flow rates, while supporting continuous chip removal. Figure 5 shows an excerpt of the high-speed recordings and a visualisation of the flow lines using PIV in the drilling head area [21]. A characteristic feature is the vortex with an axis of rotation above the outer cutting edge in the MWF, which arises due to the velocity difference and opposite flow direction, shown in the upper section in Figure 5. The supplied MWF is stopped at the bottom of the borehole and accelerated in the opposite direction due to the ejector effect. Figure 5C shows an analysis of the MWF outlet bore of the ejector drill head. In the standard drill head, the MWF emerges from the annular channel at a 90-degree angle. The velocity of the discharged MWF is significantly reduced by the overhanging boring bar. The smoothed particle hydrodynamic (SPH) simulations indicate a turbulent flow around the MWF outlet bores. The red-marked area "C.1" in Figure 5 shows that the highest fluid velocities are generated in the feed direction. The areas of lower velocities and turbulent flow behind the MWF outlet bores can be reduced by tilting the axis of the bore in the feed direction.

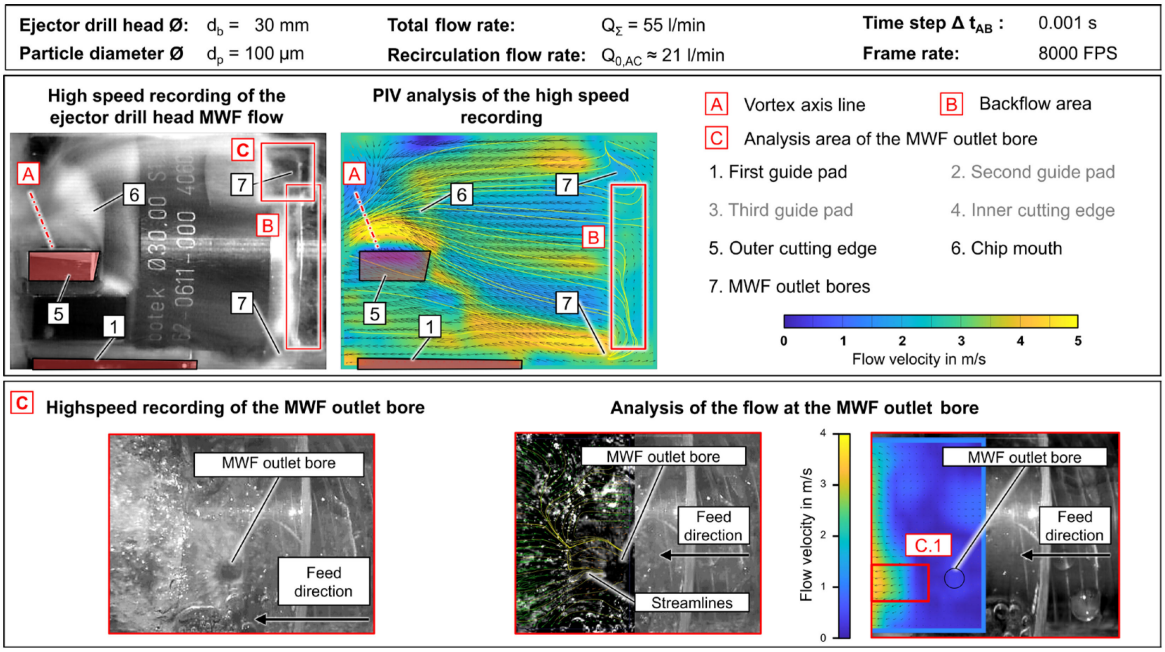

Figure 5. Analysis of the MWF flow in the area of the ejector drill head.

2.2. Discontinuous Drilling (SPP 2231-TP04)

The analysis of drilling processes in the machining of superalloys regarding the coolant supply of the cutting edges is of high importance to counteract characteristic thermal loads acting on the tool. Especially drilling high-strength materials like Inconel 718 with high thermal resistance is connected to premature tool failure resulting from high thermal loads at the cutting edge during chip formation.

The recently introduced process strategy of discontinuous drilling is an innovative approach to reduce the mentioned thermal loads in the drilling of nickel-base alloys [22]. The insertion of targeted interruptions of feed and a subsequent tool retraction out of the chip formation zone allows the cutting fluid to flush the high-loaded cutting edges. First attempts at manually inserting a periodic interruption already resulted in benefits regarding reduced tool wear and improved surface integrity [23].

However, to construe the process interruption exactly when needed to react to high temperatures efficiently before a defined temperature threshold at the cutting edges is exceeded, a coupled numerical model has to be implemented. This approach consists of a finite element method coupled with computational fluid dynamics (FEM-CFD) flow

simulation and a FEM-chip formation simulation considering the bidirectional heat transfer between the cutting fluid and the loaded solid tool and workpiece, respectively.

Initially, the FEM-CFD simulation is modelled and used for simulating the coolant flow characteristics at the cutting edges. The modelling is based on the incompressible Navier–Stokes equations. With respect to the specific process characteristics, like the high angular velocity of the tool and thus a rapidly changing computational domain, an unsuitable constant computational grid for all time steps has to be avoided. Consequently, the Navier–Stokes equations are transformed into a rotational frame of reference adopting the tool rotation. To counter the complex geometry of the twist drill, including internal cooling channels and chip flutes, the tool is modelled via the fictitious boundary method describing the fluid–solid interaction [24].

In the long term, after the successful coupling of the considered bidirectional heat transfer derived from data of the chip formation simulation, a strengthened numerical output and a temperature curve can be achieved, which allows precise estimation of thermal tool load and a parallel comparison to the stated temperature threshold. Thus, the required feed interruption to flush the cutting edges can be derived.

An exemplary discontinuous design is shown in Figure 6. The drilling process consists of a periodic interruption after an interruption distance l_U = 16 mm and is characterised by a tool retraction l_i = 2 mm and an interruption time t_i = 2 s. Regarding the actual cutting parameters, a cutting speed v_c = 25 m/min and a feed f = 0.1 mm are set.

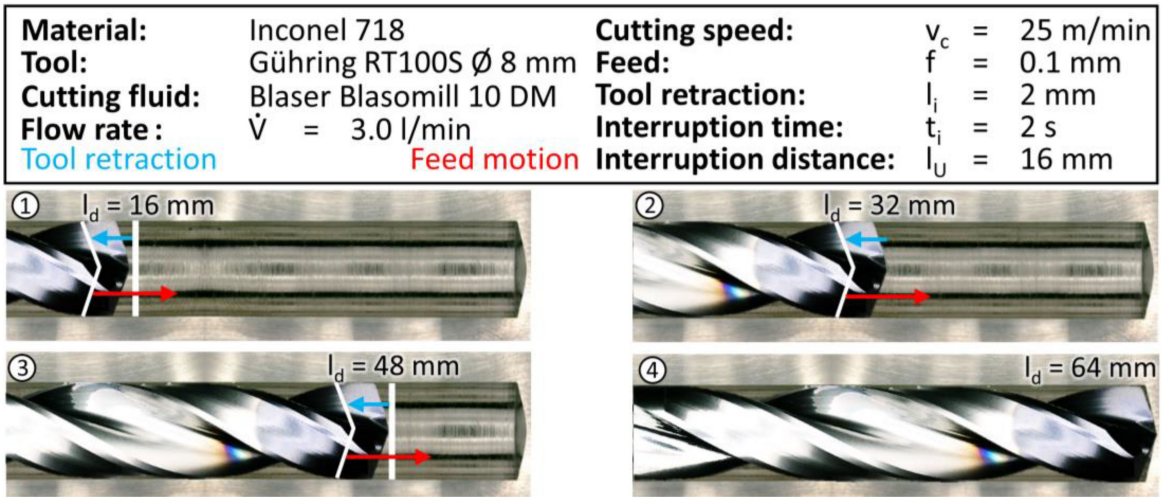

Figure 6. Visualisation of an exemplary process design of discontinuous drilling.

The mentioned CFD simulation was based on the input data of the experimentally investigated discontinuous process, such as the CAD data of the tool, cutting parameters, and material characteristics of the coolant flow, used for executing the first simulations.

Subsequently, experimental validation is required using a specified experimental setup, including a high-speed camera, which allows detailed insights into the fluid flow (Figure 7).

The high-speed setup consists a Keyence VHW-600M (Keyence, Neu-Isenburg, Germany) camera system combined with a Keyence VH-Z00R objective (Keyence, Neu-Isenburg, Germany), already used for high-speed experiments on fluid flow in ejector deep hole drilling. The incoming data during the flow analysis is processed by the high-speed camera Keyence VW-9000D (Keyence, Neu-Isenburg, Germany). The recordings were conducted with a frame rate f_R = 15,030 fps and an exposure time t_e = 1/30,000 s, resulting in a resolution A = 320 × 240 mm^2.

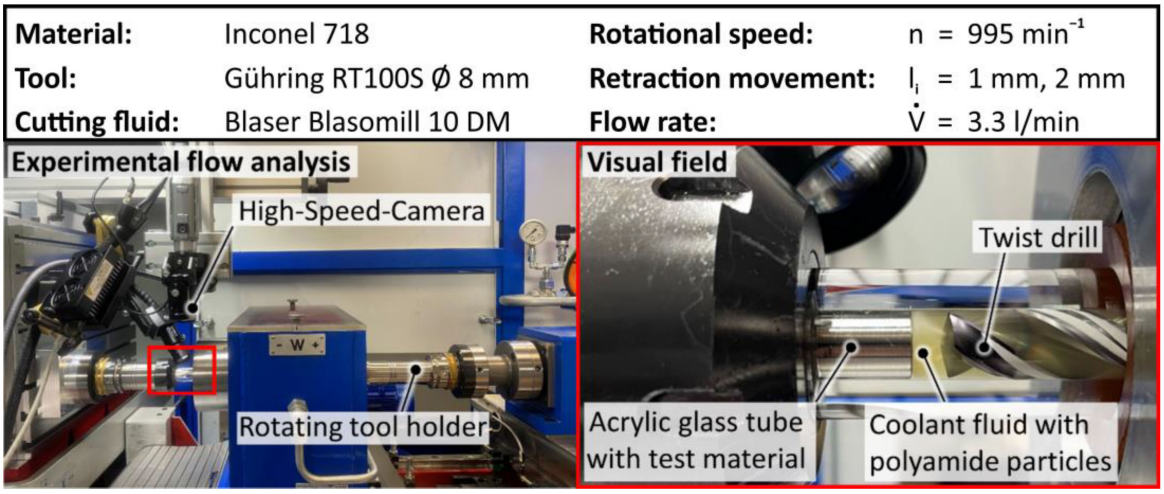

Figure 7. The experimental setup for detailed insights into flow characteristics.

For recording and analysing the flow characteristics of the cutting fluid, the test material was fixed inside an acrylic glass tube containing a drilling channel where the twist drill was arranged afterwards. The transparency of the acrylic glass tube enables the camera to focus on the visual field between the borehole bottom and the tool to analyse the flow characteristics of the fluid during the tool retraction in discontinuous drilling. To guarantee an authentic flow behaviour, the borehole bottom is contoured prior to the actual experiments and the cutting fluid is expanded by polyamide particles, which is the foundation of high-speed analysis which was also performed by Oezkaya et al. [25].

Figure 8 presents an exemplary resulting high-speed recording and, simultaneously, the first digital image processing using the open-source particle tracking velocimetry (PTV) algorithm TracTrac [26].

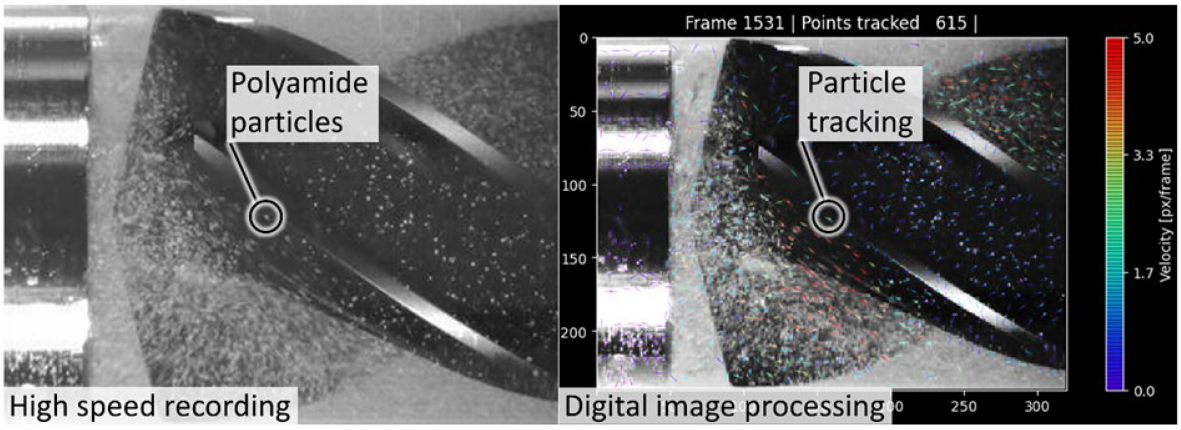

Figure 8. Raw data recordings transferred to TracTrac to analyse the velocities of the fluid.

After the single frames of a particular recording have been loaded into the environment of the algorithm, the particle tracking is carried out by going through these frames in a loop. By comparing the coordinates of the detected polyamide particles from frame to frame, velocities can be derived during the period of time in which the particle is detectable.

This described analysis of particle velocity can be seen in Figure 9, where two particles are tracked exemplarily and flow characteristics can be analysed.

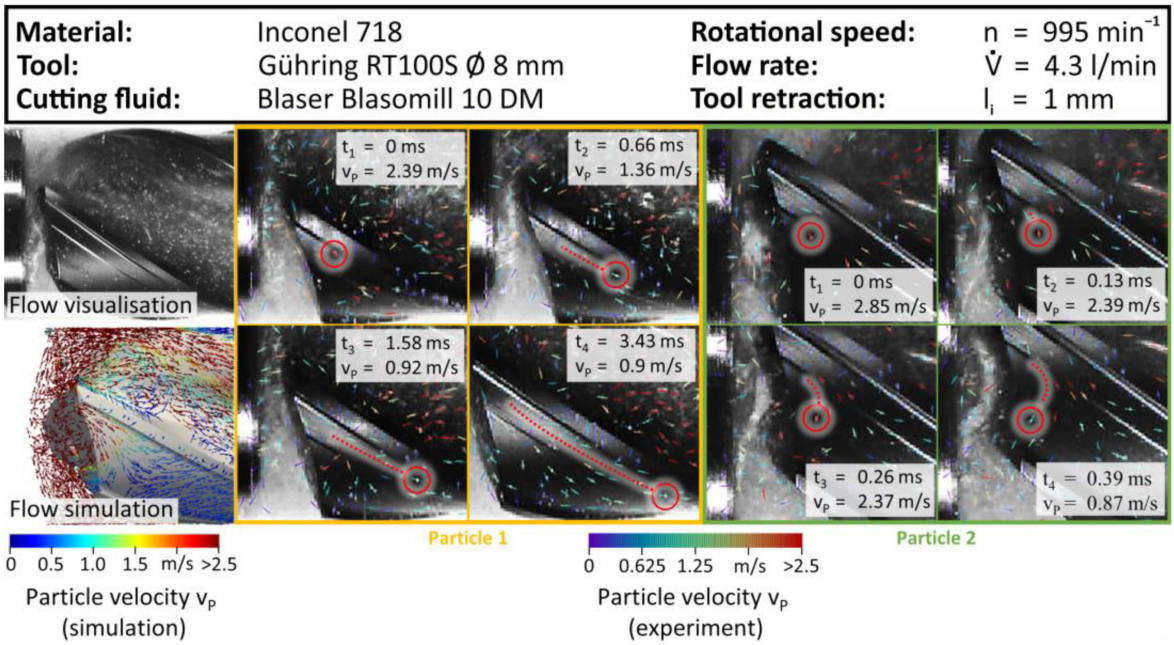

Figure 9. Particle tracking velocimetry used for identifying the flow characteristics in the coolant supply of discontinuous drilling.

The presented particle tracking velocimetry analysis focuses on validating the CFD flow simulation. Additionally, the flow characteristics of further process development derived from the CFD simulation with increased coolant pressure and decreased tool retraction were analysed. This modulation is in favour of an improved coolant supply to support heat transfer away from the cutting edges. The experimentally achieved insights into flow characteristics and measured velocities are in good agreement with the presented flow field of the simulation data. As can be seen by following particle 1, the cutting fluid is, on the one hand, transferred away from the cutting edges following the outflow caused by the principle of Archimedes' screw. However, there is also an amount of cutting fluid that is pulled back into the flute of the twist drill since a negative pressure is occurring due to high velocities acting in the area between the borehole bottom and the entry of the chip flute. Thus, the described flow behaviour, observed during the experiments on visualising the cutting fluid flow, is also in good agreement since the simulation also predicted the pull of a distinct amount of fluid back into the flute of the twist drill.

Subsequently, by comparing the flow simulation with high-speed experiments analysed by PTV, a qualified method is detected to validate numerical work on the one hand. On the other hand, the algorithm is suitable for studying the further development of flow optimisation in order to support the heat transfer from the high-loaded cutting edges into the fluid parallel to the process analysis.

2.3. Vibration-Assisted Drilling—VAD (SPP 2231-TP08)

Vibration-assisted drilling (VAD) is an innovative manufacturing process that enables the effective drilling of difficult-to-machine materials and sandwich composites [27,28], as required in various industries, such as aerospace [29]. Drilling processes can utilise MQL strategies for efficient lubrication, cooling and chip removal. In MQL, the MWF is dispersed as an aerosol and directly transported into the drilling site through cooling channels within the drill bit. It has been observed that for Ti-machining with internal MQL application, temperatures in the workpiece are reduced by 50% compared to conventional MQL application via external channels [30]. Qualitative analyses of air pressure, gas–liquid ratio, cutting parameters, and MWF mist concentration are currently ongoing, while mist diffusion and quantitative mapping of the relationship between operating conditions and MWF mist concentration remain to be investigated [31]. Shadowgraph visualisations were

performed to analyse the MQL flow dynamics at the twisted drill bit exit. In addition, a digital image analysis (in Python) was developed for further detailed investigations. These allowed the mapping of specific flow regimes across different operating conditions.

2.3.1. Materials and Methods (VAD-TP08)

Figure 10 shows an overview of the VAD process with details of the MQL mist generation and delivery to the working area.

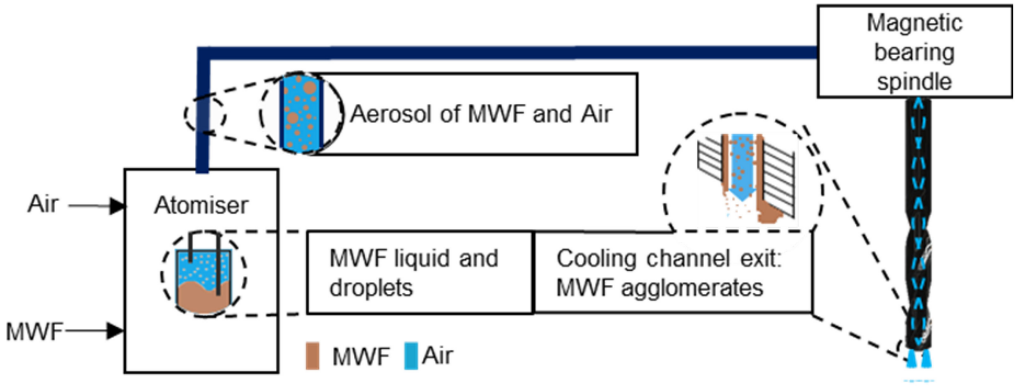

Figure 10. Setup for vibration-assisted drilling using MQL with an atomiser for aerosol generation and active magnetic bearing spindle for vibration.

Using a Breeze LSJ Z30 air spray injector (HPM Technologie GmbH, Dettingen an der Erms, Germany), the air is pressurised and pumped into the MWF tank containing Setral Alumicut 659 synthetic oil (Setral Chemie GmbH, Seeshaupt, Germany). A Venturi nozzle atomises the MWF by accelerating the airflow and simultaneously reducing the pressure, resulting in a fine mist that enters the pipes towards the LeviSpin spindle (Keba, Givisiez, Switzerland). The drill bit (Ceratizit Group, Mamer, Luxembourg) is made of TiAlN-coated solid carbide with a diameter of 8 mm and two internal spiral channels with an internal diameter of 1 mm. Numerical simulations were performed to investigate the MQL multiphase flow inside the internal channels of the drill bit [17]. Assuming the MQL air/oil aerosol has a mean droplet diameter of 5 µm, the Stokes number of such a droplet flow regime is St > 10, according to Equation (1):

$$\mathrm{St} = \frac{\rho_{MWF} \cdot d_{MWF}^2 \cdot U_{air}}{18 \cdot \mu_{air} \cdot d_{channel}} \quad (1)$$

In general, St > 1 does not allow the droplet trajectories to follow the gas flow. Consequently, the droplets deviate from the airflow inside the spiral drill bit channels and hit the inner walls, creating an MWF wall film, as shown in [17]. An active magnetic bearing spindle generates the vibration according to low-frequency vibration-assisted drilling at frequencies between 10 and 200 Hz [32]. In situ measurements of the MWF flow in the work area during drilling are challenging. Surface quality and tool wear, as well as force and temperature measurements, can provide some insight into the processes occurring in the borehole. However, to directly observe the flow of the MWF, as shown in Figure 11, the drill bit is placed between a high-speed camera and a light source, thus operating in shadowgraphic mode.

To analyse the MWF as it leaves the cooling channels, recorded images were analysed using a Python code with the following steps: First, a background video recorded without MWF is subtracted from the MWF video, keeping only the MWF-related pixels, followed by a binarisation of the greyscale image using a light intensity threshold. The resulting black-and-white images can be further processed to quantify the spatial and temporal dynamics. It was assumed that the key dynamics of the MQL flow can be characterised by analysing the flow over a line close to the drill (see Figure 11C). This allows the MQL

dynamics to be plotted in a spatiotemporal diagram, which can be further analysed using mathematical methods.

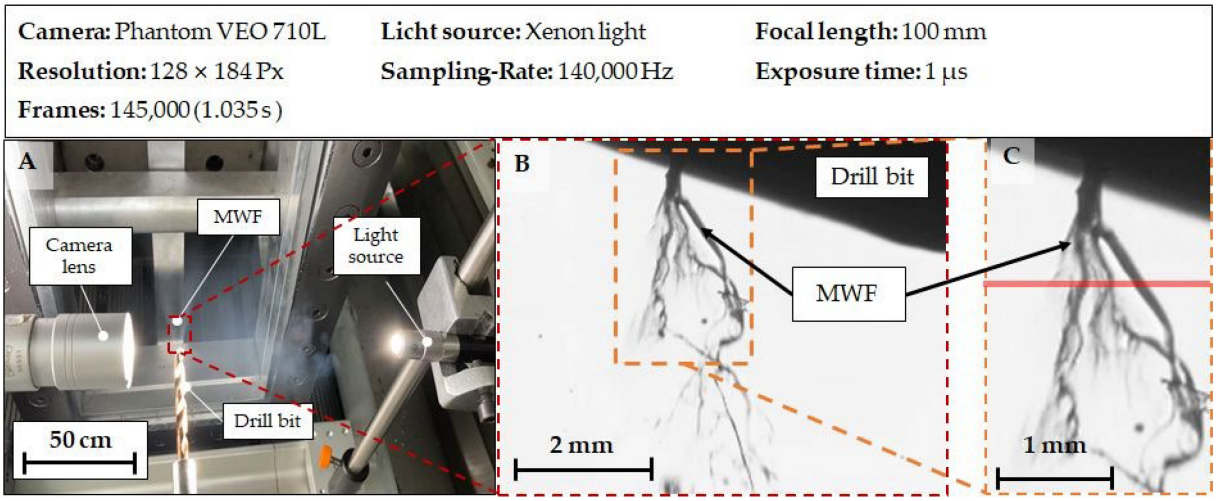

Figure 11. Experimental setup (**A**) of shadowgraphic imaging for MQL exiting the internal channel; (**B**) MWF exits the drill bit, and its shadow at one of the cooling channel exits is captured; (**C**) along the red line, a detailed spatiotemporal analysis is performed to characterise the flow dynamics.

The position of the detection line is selected to be below the drop-like MWF agglomerates formed by the MQL flow, thus allowing an analysis of the ejected MWF.

2.3.2. Results and Discussion (VAD-TP08)

Analysis of the image sequence of 56 combinations of air and oil input pressures identified three distinct flow regimes. Figure 12 shows the number of dark pixels and, therefore, MWF in the line of interest over 50 ms for an example parameter set from the drop-like regime. In Figure 12A, a sequence of cutouts of raw images over 31 ms shows the accumulation of MWF agglomerates in this regime. The lowest drop frequency was analysed with a fast Fourier transformation (FFT) of the time series and determined to be 23 Hz with 6 bar air input and 3 bar MWF.

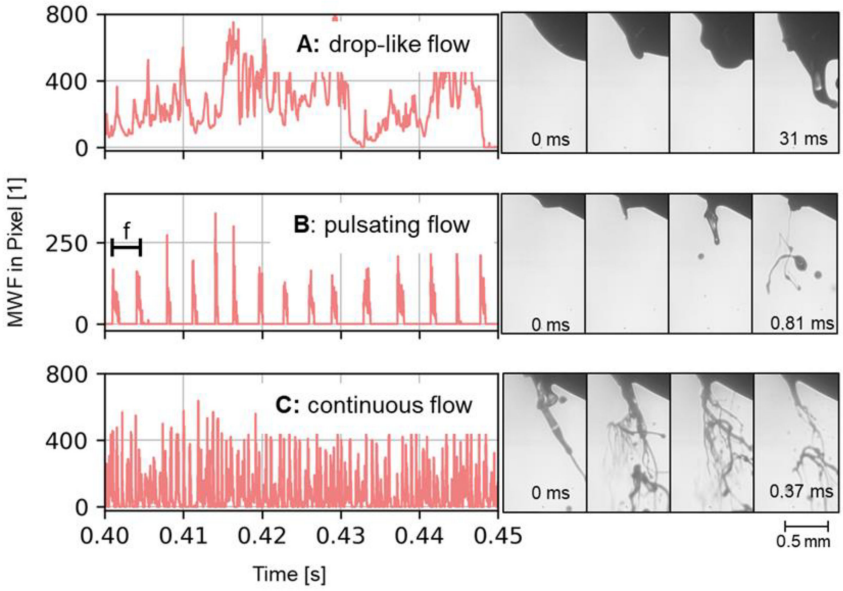

Figure 12. Examples of evaluated MWF pixels for the three flow regimes (**A**–**C**, red lines) over 50 ms with the frequency f shown in B, and cutouts of image sequences showing single events from every regime.

In the pulsating flow regime, depicted in Figure 12B, the peaks are much more distinct. The frequency of MWF application, as shown in Figure 12B for input pressures within this regime of 9 bar for air and 4 bar for MWF, was calculated to be 444 Hz. MWF agglomerates are still present at the exit of the cooling channels, as reported by Stampfer et al. [33], and the high-velocity airflow often tears the MWF film away from the drill bit tip, resulting in secondary atomisation. Figure 12C shows the continuous regime. The formation of ligaments and secondary atomisation is clearly observed in the sequential images between 0 and 0.37 ms of the process.

To generate a regime map of the MQL flow behaviour over the operating conditions of air and MWF, the input pressures were analysed, as shown in Figure 13.

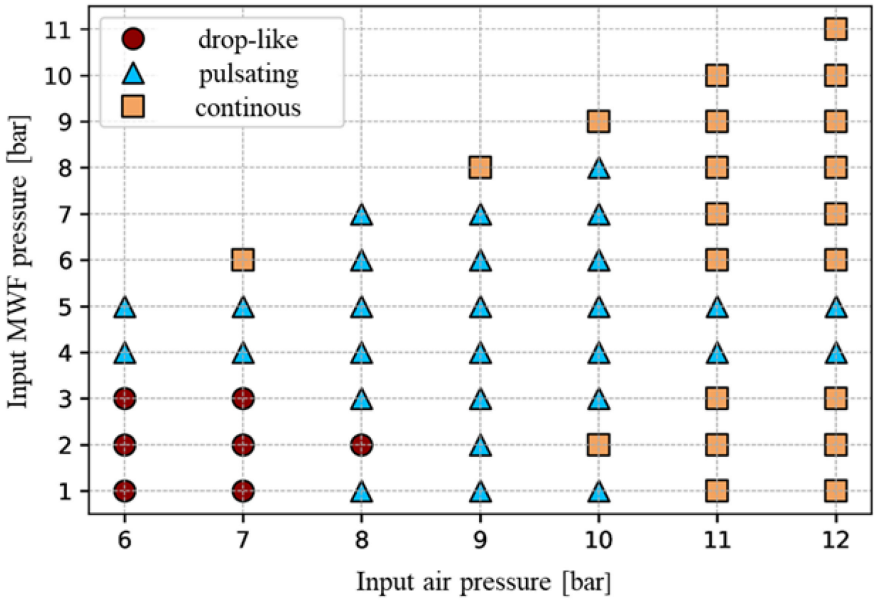

Figure 13. Input air, MWF pressure, and the resulting flow mapped, showing drop-like flow at low input pressures, pulsating, and continuous flow.

Input pressures of 6 and 7 bar for air and 1, 2, and 3 bar for MWF show the aforementioned distinct flow pattern with rather big agglomerations of MWF at the channel exits separating in a drop-like manner. At higher input pressures, a pulsating flow with a high number of separated events can be seen. The highest operating pressures lead to ligaments of MWF continuously exiting the internal channel. The presence of drop-like, pulsating and continuous regimes in the distribution allows the type of flow to be determined by the choice of input pressures. In VAD, the cutting process is periodically interrupted, resulting in the production of relatively short chips rather than long helical chips. Therefore, to ensure that each cutting operation is efficiently lubricated, it is important to know not only the MWF requirements but also its spatial and temporal application in the process. In low-frequency VAD with a vibration frequency of 25 Hz, a drop application frequency of about 23 Hz, as found for 6 bar air and 3 bar MWF, can result in unlubricated cuts.

2.3.3. Summary (VAD-TP08)

Shadowgraph imaging of MQL using a static twisted drill bit was used to investigate the MWF exiting the internal cooling channels over input air and MWF pressures. The flow behaviour was quantified using script-based evaluation, and the frequency of MWF application was determined for sample input pressures.

Three different flow regimes were found with drop-like, pulsating, and continuous flow and different MWF application frequencies. Therefore, it can be concluded that depending on the input pressures and vibration frequency selected, MWF is either applied continuously only a few times between two cuts or only once every few cuts in the drilling substrate.

In a practical drilling operation, the oil and air input pressures and resulting flow regimes can be used to set a desired MQL flow behaviour as long as the same setup is used. The next steps, such as determining the volumetric flow rate of the air and MWF, will allow the findings to be transferred to different machining processes.

A static setup without rotational forces was used. Dasch and Kurgin [8] found that the dual channel internal MQL was not only more effective in chip removal compared to the single channel and external MQL but also that the mist levels were not significantly affected by the spindle speed.

The experimental data presented here can be used to validate computational fluid dynamics simulations, which in turn can be extended to include rotation using dynamic mesh motion.

2.4. Circular Saw with Internal Coolant Supply—ICS (SPP 2231-TP09)

Circular sawing is an important metal-cutting technique for manufacturing semi-finished products. A saw kerf is created during the cutting process. As a result, the cutting process mostly occurs in a narrow, almost closed tooth gullet in the saw kerf. This makes it difficult to reliably deliver the cooling lubricant to the cutting process using an external flood lubrication system. Using holes in the circular saw blade makes it possible to directly and reliably deliver the MWF to the saw kerf. This internal coolant supply can reduce the thermal tool load and increase component quality [34]. Similar effects have also been observed in turning [35] and milling [36].

When the cooling lubricant flows into the tooth gullet in the kerf, it interacts with the forming chip. Therefore, it is of interest to find out how the flow field is formed in the kerf. Figure 14 shows an experimental setup for investigating the flow properties and the interaction of the chip with a cooling lubricant during circular sawing. The overall process was reduced in complexity here [37]. This included a simplification of the kinematics. In the actual circular sawing process, a cutting edge performs an elliptical cutting motion (superimposed rotation and translation). This makes it challenging to observe a single tooth with a measuring device such as a high-speed camera. Therefore, the kinematics were reduced to a stationary tool and a moving workpiece in a linear cutting process. For this purpose, two-toothed segments were cut out of the circular saw tool and clamped into a tool holder in a special test stand. By using two-toothed segments, it was possible to maintain the condition of a closed tooth gullet. The test stand performed a linear cutting motion designed for basic investigations into orthogonal and oblique cutting. To visualise the cutting and flow processes, the saw kerf was modelled by putting up sapphire glass on both sides (the safe distance between the tool and the sapphire glass was 0.05 mm). The workpiece was clamped between the two pieces of sapphire glass. The process was recorded in the x–y plane (Figure 14) employing a high-speed camera (type IDT OS8, Integrated Design Tools, Inc., Pasadena, CA, USA) and appropriate lighting. The cooling lubricant was provided by an external pump connected to the tool holder system. The tool used was a circular saw blade (type Tube Cut, AKE Knebel, Balingen, Germany) with a diameter of 350 mm, a width of cut of 2.7 mm, a blade thickness of 2.5 mm, and z = 80 number of teeth. A hole of ⌀1.5 mm was made in the tool. Water was used as a cooling lubricant for better visualisation conditions.

Figure 15 shows a comparison of chip formation processes for different fluid settings. A 2.8 mm wide and 100 mm long rectangle made of Ti6Al4V was used as a workpiece. The tests were conducted at a cutting speed of v_c = 40 m/min and an uncut chip thickness of h = 0.05 mm. Figure 15a shows a dry cutting process. The chip filled most of the chip space when curling up. As the chip continued to pour in, it finally buckled, and a chip tangle was formed. This was caused by insufficient lubrication of the chip space and may lead to a deterioration of the machining surface and a load on the tool due to chip jamming. Using an internal coolant supply through the two-toothed segment showed that the chip curling was influenced. It could be seen that increasing the volume flow from 1.5 L/min to 2.5 L/min led to a considerable improvement in chip curling. This was due to the interaction between

the chip and the fluid. The chip-forming process could thus be improved by the mechanical force exerted by the fluid on the chip and by favourable flow conditions in the chip space.

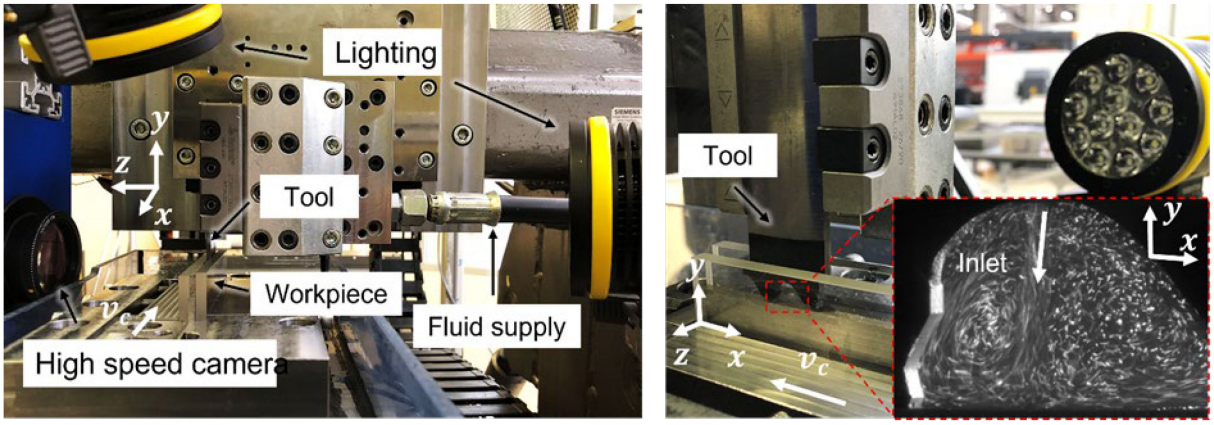

Figure 14. Test stand for cutting tests with a two-toothed segment and internal coolant supply.

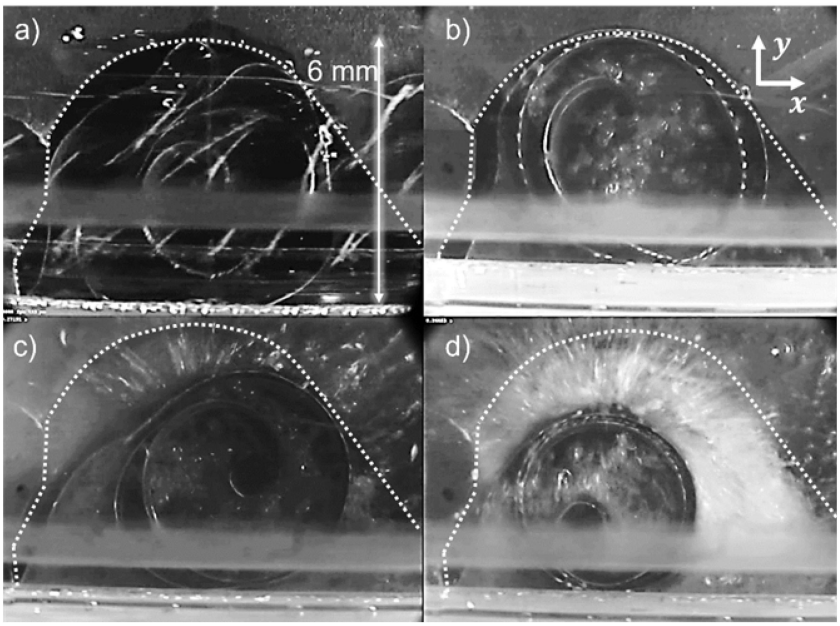

Figure 15. High-speed images taken at v_c = 40 m/min and h = 0.05 mm; (**a**) dry; (**b**) ICS with 1.5 L/min; (**c**) ICS with 2 L/min; (**d**) ICS with 2.5 L/min.

As the tooth gullet is relatively small and the saw kerf is difficult to access by a measuring device, an analogue test was developed to model the fluid dynamics in the tooth gullet of the saw kerf (Figure 16). In the analogue test, the two-toothed segment shown in Figure 14 was used as a basis. The geometry of the saw tooth was enlarged by a factor of ten. Thus, the characteristic parameter (the diameter of the supply hole) was also increased by a factor of ten. To keep the fluidic properties of the system, the Reynolds number was kept similar, between Re = 21,200 and 35,300. By reducing the flow velocity by a factor of ten, it was possible to adapt the Reynolds number to the original system. Water was again used as the test fluid so that the material properties, such as density and viscosity, were not changed. The fluid was provided to the system via an external pump. The volume flow was set to 25 L/min (Re = 35,300) using a controller. Polyamide particles with a diameter of 90 µm were added to the fluid to visualise the fluid movement. High-speed images were recorded with an IDT OS8 camera in the x–y plane.

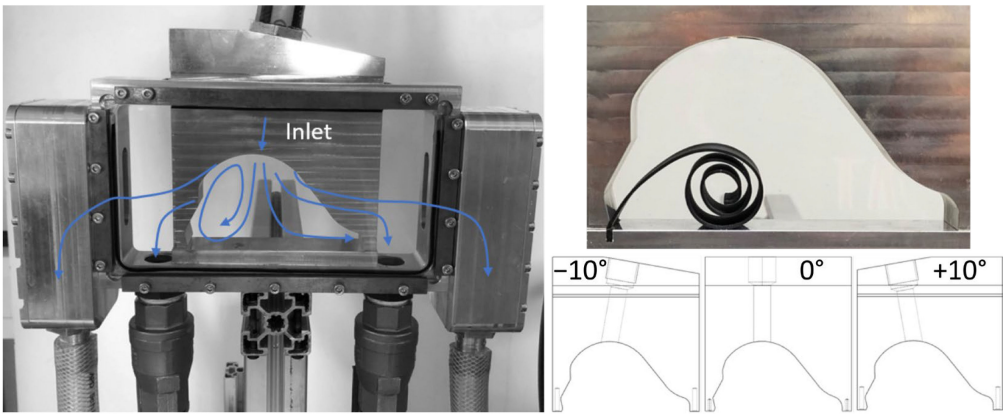

Figure 16. Analogue test stand for flow experiments with and without chips as well as with three different angles of supply holes. The arrows (left side image) indicate the flow direction.

The empty tooth gullet was taken into consideration first. Three different inflow angles were selected (−10°, 0°, and +10°). In order to examine the influence of a chip in the flow field, a chip was additively manufactured and fixed in the chip space. The size and the form of the chip were measured in the high-speed images of the cutting tests. The fluid dynamics were recorded at a frame rate of 12,000 fps and evaluated with the TracTrac PTV software [26]. This open-source MatLab/Python code made it possible to examine the polyamide particles in the flow field utilising particle tracking velocimetry (PTV). Thus, the high-speed images could be used to quantitatively and qualitatively evaluate the flow properties in the saw kerf for the sawing process.

Figure 17 shows the velocity fields of the components u and v in the x–y plane for the empty chip space (without chip) for three different inflow angles (−10°, 0°, and +10°). It is evident that two dominant vortex structures were generally formed. Depending on the inflow angle, the shape and the size of the vortex structures changed. The actual chip-forming process took place in the bottom left-hand corner. Thus, the dominant heat source was located there. Therefore, an inflow angle of 0° and +10° was more favourable for the cooling of the cutting edge since the narrower vortices caused a better rotation throughout the chip-forming area.

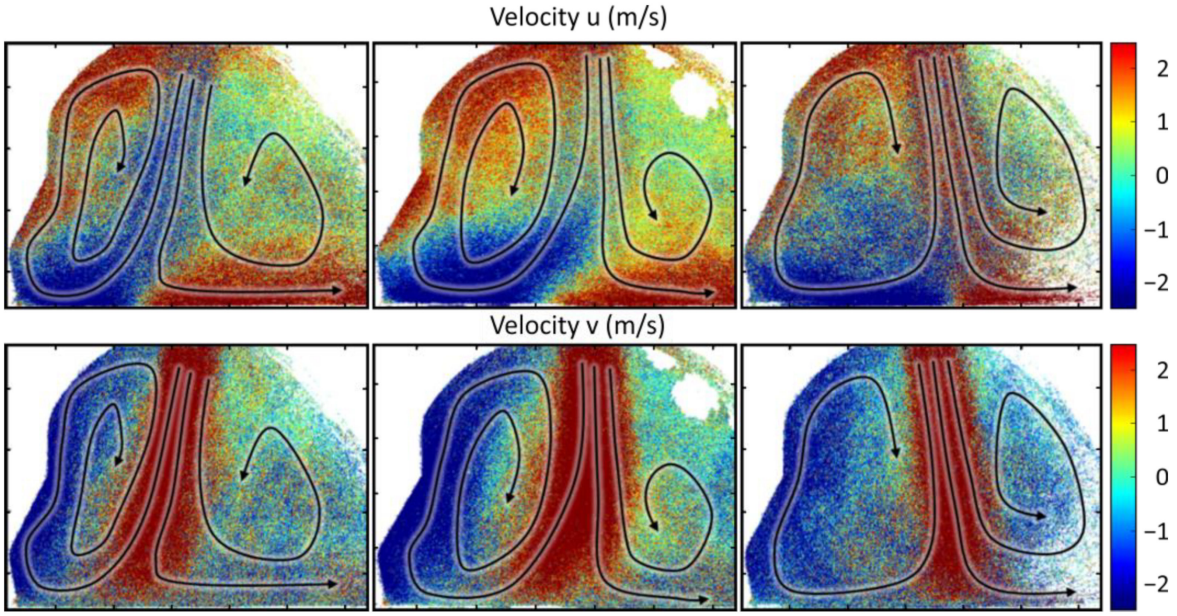

Figure 17. Velocity components u and v for different supply hole angles of −10°, 0° and +10° in the empty chip space. The arrows indicate the flow direction.

If there was a chip in the flow field, the influence of the inflow angle became clearer. When the fluid flow met the chip, the fluid was deflected (Figure 18). An inflow angle of +10° showed a clear rotation around the chip. Most of the fluid flowed toward the chip-forming area (on the left). Hence, there was still a good supply of cooling lubricant for the chip-forming process. Even at an inflow angle of 0°, there was a good supply of cooling lubricant due to a fluid flow in the direction of the chip-forming area. However, at an inflow angle of −10°, the cooling lubricant could not be provided very well to the chip-forming area. In the empty chip space (Figure 17), the cooling lubricant clearly flowed in the direction of the chip-forming area after the inflow had reached the workpiece surface. This flow was weakened and prevented by the chip.

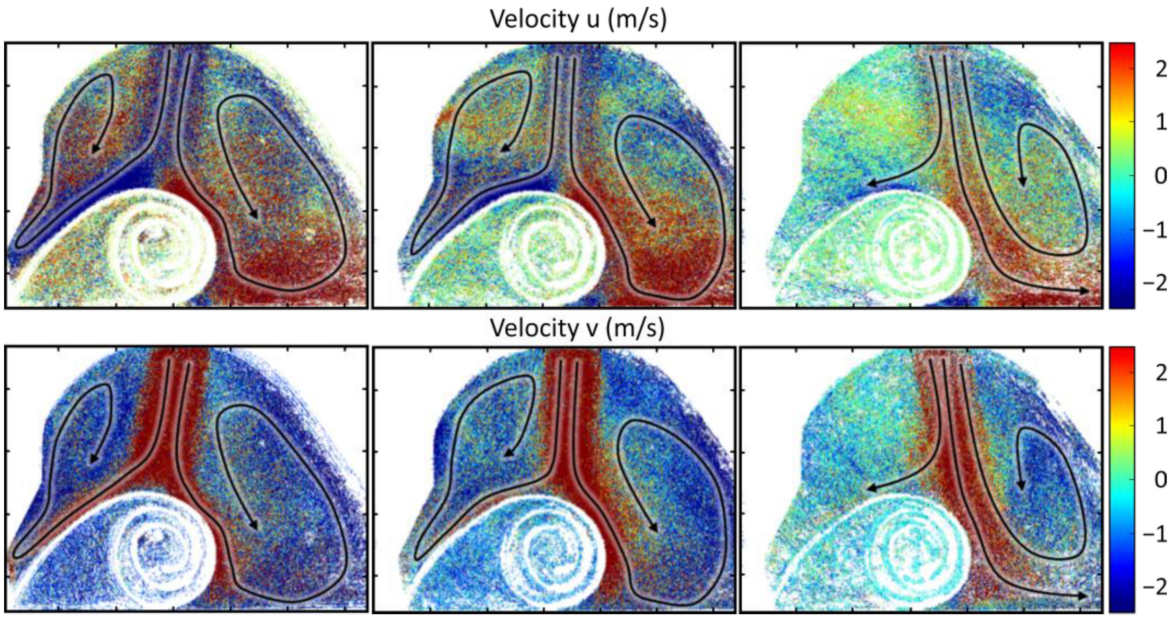

Figure 18. Velocity components u and v for different supply hole angles of −10°, 0°, and +10° with the chip. The arrows indicate the flow direction.

The flow behaviour in the chip space and the narrow kerf during circular sawing was investigated with two test setups. In the first test, it was shown that an internal coolant supply clearly influenced the chip-forming process (especially the curling). While the chip folded up and rolled in randomly in dry cutting, a controlled chip movement was achieved with ICS. This increased not only the process stability but also avoided jamming the chips and damaging the cut surface. In a second test setup, the flow properties were investigated in greater depth. For better accessibility of the measuring device, a test setup with a similar Reynolds number was created. The original saw tooth was enlarged here by a factor of 10. By using polyamide particles, it was possible to examine the flow field in the chip space using high-speed film recordings. Three inflow angles (−10°, 0°, and +10°) were taken into account. Furthermore, the influence of a chip on the flow behaviour was examined by adding an additively manufactured chip. Finally, the velocity fields in the components u and v were evaluated by PTV. It was concluded that the inflow angle significantly influences the flow formation in the tooth gullet. In general, an inflow angle of +10° is preferable, as this creates a favourable vortex in the direction of the chip-forming area. Even if a chip is in the flow field, the inflow of +10° is advantageous. However, an inflow angle of 0° shows an almost similar and equally advantageous flow field. In view of the considerable technical challenge of inserting supply holes in a circular saw blade, the variant with 0° appears to be best from the perspective of a cost–benefit assessment.

2.5. Precise Electrochemical Machining—PECM (SPP 2231-TP10)

Electrochemical machining (ECM) is an efficient method utilised for machining high-strength materials like nickel-based alloys. Figure 19 (left) shows the setup schematic of the process. ECM ensures high surface quality without thermally or mechanically damaging the rim zone [38,39]. ECM is commonly employed in the production of turbine components, such as blades [40,41]. Precise electrochemical machining (PECM) is a widely used variant of ECM for achieving high precision and superior surface qualities during finish machining. In PECM, a mechanical oscillation is applied to the tool electrode, leading to a temporary variation in the working gap size. An electrical pulse is applied at the bottom dead centre of the mechanical oscillation, where the gap size is the smallest. This combination allows for attaining high current densities and reduced working gaps, typically around 10–100 µm, resulting in surface roughness of Ra $\geq$ 0.03 µm [42,43].

PECM takes advantage of both the tool oscillation and pulse-off times to facilitate the efficient renewal of the electrolyte within the working gap. However, industrial applications have shown that mechanical tool oscillation and flushing pressure can result in workpiece deflections, primarily in thin-wall geometries like turbine blades. These deflections are attributed to fluid–structure interactions (FSIs) and are responsible for process instabilities. To mitigate this, an often-used approach is to decrease the electrolyte flushing pressure and mechanical oscillation frequency, albeit at the cost of sacrificing some of the available technological potential for achieving higher productivity [44].

To minimise these induced workpiece deflections and local gas agglomerates in the working gap that reduce the imaging accuracy of the process, a fundamental understanding of the related phenomena is required. To this end, experimental in situ measurements of the gas transport during ECM are presented in this section. The measurements are based on the upscaled test bench proposed by Rommes et al. [45] and developed by Tchoupe et al. [44]. Measurements are performed using particle image velocimetry (PIV), a non-intrusive optical technique characterised by high spatial and temporal resolutions [46]. Detailed knowledge of the behaviour of the bubbles and their hydrodynamics during machining is indispensable to develop efficient and deterministic decision models for the selection of optimal machining parameters. The decision model considers the target product characteristics and the starting workpiece properties, as shown in Figure 19(right).

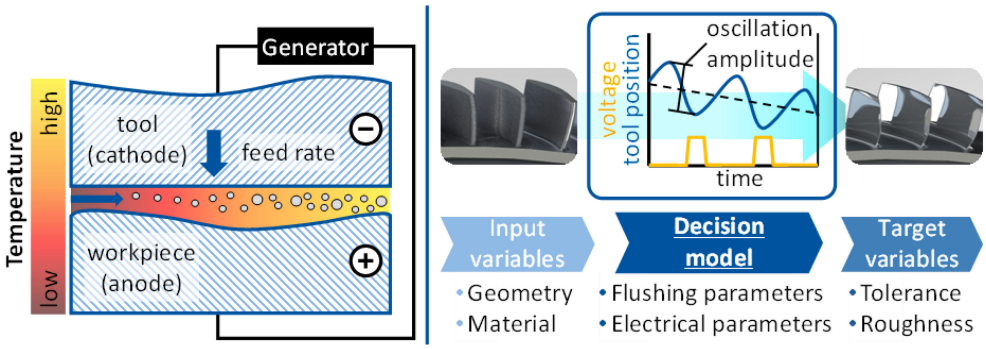

Figure 19. Material removal principle of electrochemical machining (**left**), based on [47], and the concept of decision model (**right**) as proposed by Rommes et al. [45].

2.5.1. Concept and Experimental Setup (PECM-TP10)

The upscaled approach for in situ measurements of the gas transport in PECM [44,45] aims to circumvent the limitations imposed by the typical small working gaps observed in (P)ECM (0.05 to 0.5 mm). Scaling is based on the principle of dynamic similarity, according to which two fluid flows will be identical if they have similar setups (similar shapes with different sizes) with identical boundary conditions and the same Reynolds number. Upscaling the gap allows access to a suitable light source and cameras such that

the instantaneous flow field of the electrolyte and gas bubbles mixture can be analysed using PIV measurements.

Based on the requirements of the PIV measurement approach, an upscaled factor of 100 of the actual PECM working gap was selected. This corresponds to a test bench with a gap of h = 10 mm. In order to keep the Reynolds number constant, other flow properties such as the flow velocity, flow rate and pressure drop must be reduced by the corresponding factor. The real process parameters, as well as those for the upscaled test bench, are shown in Table 1 [44], and the experimental setup is shown in Figure 20.

Table 1. Upscaled setup of process and optimised parameters.

Process Variables	Real Process	Experimental Setup
Working gap, s (mm)	0.1	10
Flow velocity, v (m/s)	15–50	0.15–0.5
Volume flow rate, Q (L/min)	0.45–15	45–1500
Bubble diameter, d_b (mm)	0.001–0.01	0.1–1
Pressure drop, p (bar/m)	200	2×10^{-4}

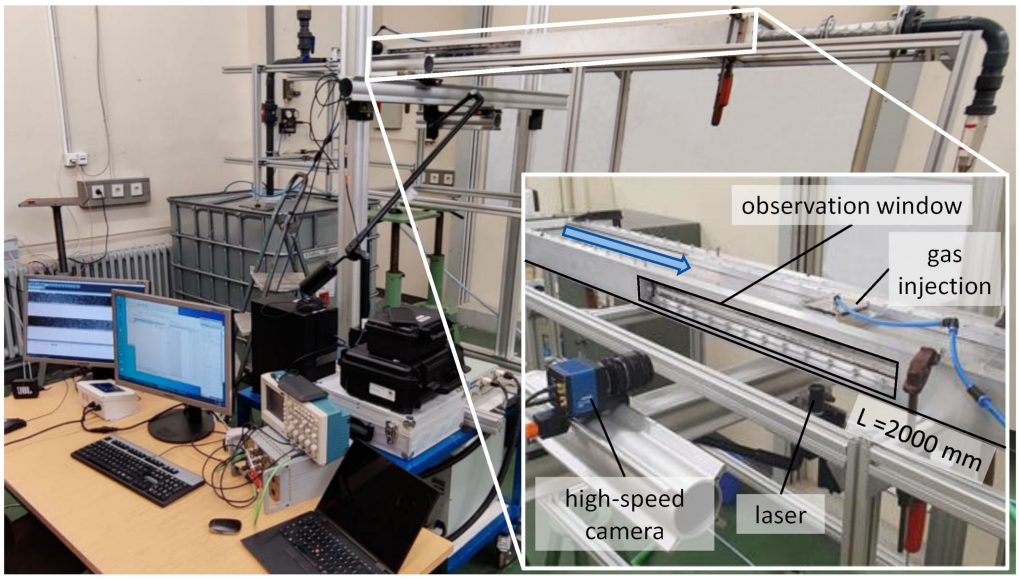

Figure 20. Flow channel of the experimental setup with PIV measurement gear.

Hydrogen bubbles in ECM and process variants result from electrolysis. In this regard, realising the typical gas fraction of α_g = 20% for an electrolyte flow rate of Q_{real} = 45 L/min in the upscaled test bench will require peak currents of up to $I_{p,exp}$ = 40,000 A according to Faraday's law. Since this extremely high electric current requirement cannot be attained, gas bubbles are seeded using a gas sparger, as shown in Figure 21 (left and right) below [44,48]. The sparger is built in such a way that the diameter of the bubbles is determined by the porosity of the membrane.

PIV measurements were conducted at a distance of x = 1300 mm downstream to capture the flow field, both for the single and multiphase flow. For the measurements, the flow was seeded with red fluorescent polymer microspheres with a mean diameter of d_{tracer} = 50 µm and a mass of m_{tracer} = 100 g. A double-pulsed Nd:YAG laser with a wavelength of λ = 532 nm and a maximum energy per pulse of 25 mJ was used to illuminate the tracer particles. The light sheet had a thickness of approximately t_{laser} = 0.5 mm and covered the total channel height in the downstream direction. A pco.panda 26 DS camera (Excelitas PCO GmbH, Kelheim, Germany) with a 5120 × 5120 pixels sensor was used,

installed perpendicular to the measurement plane and equipped with a 105 mm Nikon lens (Nikon, Tokyo, Japan). Images were acquired with a pulse separation time of 300 µs.

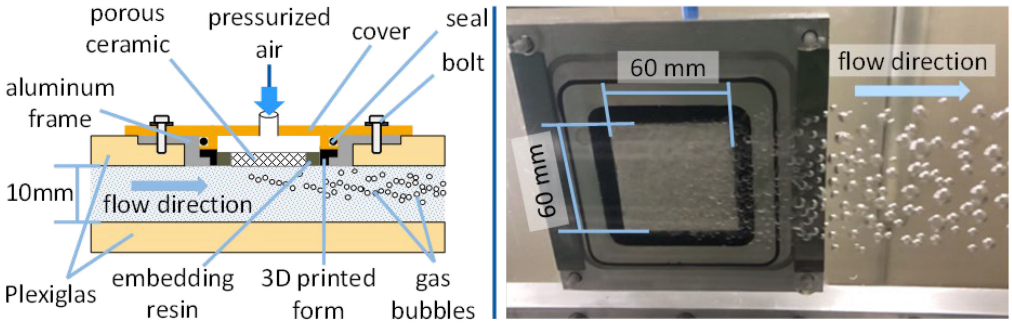

Figure 21. Gas seeding approach based on porous ceramic material (**left**) and photo of produced bubbles in the flow channel (**right**).

2.5.2. Measurement Results (PECM-TP10)

Prior to performing multiphase flow measurements, the fully developed channel flow conditions for single-phase flow were validated using direct numerical solutions (DNS) [44]. In the next step, gas bubbles were injected through the sparger with different flow rates corresponding to gas volume fractions of α_g = 10% and 20%. As seen in Figure 22 (left), the injected gas bubbles remained mainly near the top surface, through which the gas bubbles were injected. This accumulation of gas bubbles can lead to the total insulation of the cathode in the real process, which is avoided by pulsing the electric current supply. In the pulse-off time, the electrolytes in the working gap can be renewed. In addition, the figure shows that the bubbles coalesced strongly within a few channel heights after they were formed, resulting in diameters of up to 20% of the channel height. Figure 22 (right) shows the gas bubble penetration depths for α_g = 10% and 20% at Re = 5200. It was observed that greater depths correlate with higher accumulated gas fractions in the working gap. A qualitative comparison of the bubble penetration profile with in situ observations of the working gap during machining [47] showed agreement.

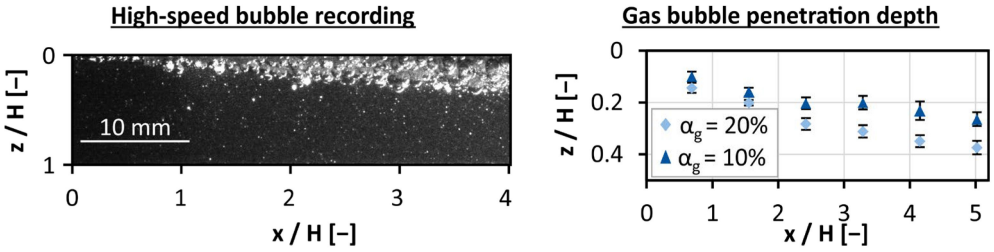

Figure 22. Snapshot of the injection of bubbles into the channel (**left**) and vertical bubble penetration depth as a function of the coordinate x along the channel axis (**right**).

Figure 23 shows the contours of the averaged streamwise velocity component derived from 100 PIV measurements. The PIV algorithm could not distinguish between tracer particles and bubbles in the bubble-dominated regions of the flow. This means that compared to the lower half of the channel, which is mostly occupied by water alone, the velocity in this area mainly represents the velocity of the bubbles. Consequently, the oscillation of the tool is used in the real process to improve the removal of gas bubbles in this region.

2.5.3. Summary and Outlook (PECM-TP10)

Gas transport phenomena in PECM remain an area of limited scientific understanding due to the lack of suitable experimental investigations. In this work, the gas transport during ECM was observed using an analogy test bench consisting of an upscaled working gap based on dynamic similarity. It was observed that regions with high concentrations of

gas bubbles have lower velocities. Further, these bubbles tend to coalesce in these regions. In the future, the current test bench should be extended to a channel with moving walls. This is necessary to capture the bubble movement induced by tool oscillation during PECM.

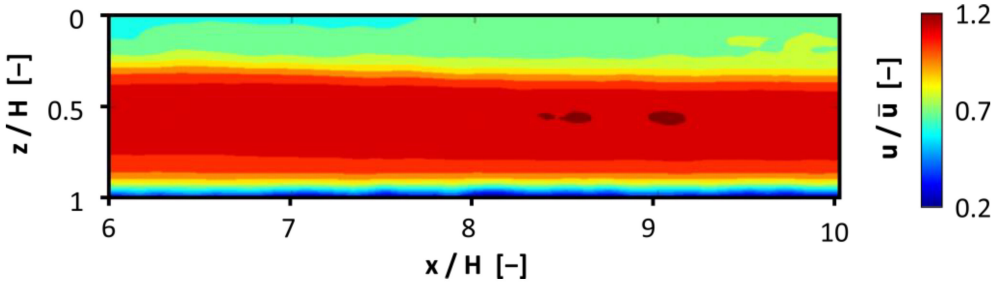

Figure 23. Normalised axial velocity from the PIV measurements for a multiphase flow at Re = 5200 and α_g = 10% [44].

2.6. Machining with Flood and Jet Cooling (SPP 2231-TP11)

Precise characterisation of liquid jets used during machining with flood and high-pressure cooling techniques is a highly complex task. The moving parts and lack of fixation places make it hard to position the necessary measuring devices. In addition, the enormous amount of liquid splashing due to contact with the tool and workpiece may completely block the optical access to the region of interest. For that reason, in this work, only free jets, i.e., jets not disturbed by any obstacle, were analysed. Three different cooling systems were studied, of which two are used in flood cooling and the other is used in high-pressure cooling. Also, different pressures were used to control the flow rate in each nozzle.

The main difference between the nozzles in the present study is the geometry of the internal channel. Nozzle 1 has a smooth internal channel and can be bent in order to adjust the impinging angle depending on the tool and workpiece. Nozzle 2 (outlet piece), on the other hand, has a screw shape internally and can have the impinging angle adjusted by rotation. System 3 consists of a combination of three nozzles. Two of the nozzles are located on the top and have a diameter of $d_{HPC,top}$ = 1.2 mm, and one is located on the bottom and has a diameter of $d_{HPC,bottom}$ = 1.4 mm. All three nozzles are oriented towards the tip of the cutting tool, which corresponds to the region of elevated heat transfer during the machining process.

A photo of the experimental setup used for the flow visualisation is shown in Figure 24a. Pressure sensors of type A-10 (WIKA Alexander Wiegand SE & Co. KG, Klingenberg, Germany) were used to measure the pressure prior to the flow outlet. A high-speed camera of type FASTCAM SA4 (Photron Deutschland GmbH, Reutlingen, Germany) was positioned inside a turning lathe TNX 65 (TRAUB Drehmaschinen GmbH & Co.KG, Reichenbach an der Fils, Germany) to record the free jets. An LED array was used as a backlight with a diffuser plate, which ensures uniform illumination. In order to avoid in-motion unsharpness, shorter exposure times are also required, reducing the time that the camera sensor is exposed to light [49]. However, the camera sensor needs a certain amount of light to capture meaningful images. Therefore, the extra illumination provided by the LED array compensates for the reduction in exposure time by increasing the light intensity. To complement the illumination setup, a high-power LED was used as the front light, allowing visualisation of the jet structures. The resulting images captured by the high-speed camera can be seen in Figure 24b, obtained with a framerate of f = 3600 fps and an exposure time t_e = 1/108,000 s. In Figure 24c, the importance of having an adequate exposure time and framerate is highlighted by showing the resulting image, for the same system, with f = 50 fps and t_e = 1/100 s. This image provides information on the time-averaged structure of the jet, but no velocity information can be extracted from such images.

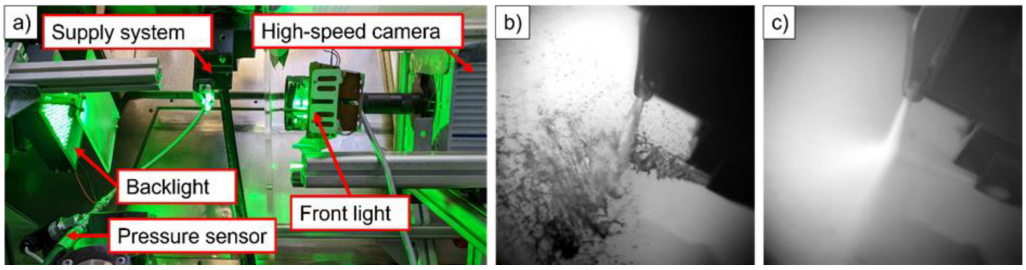

Figure 24. (**a**) Experimental setup used for flow visualisation: (**b**) image of system 3 captured by the high-speed camera at f = 3600 fps and exposure time t_e = 1/108,000 s; (**c**) image of system 3 captured by the high-speed camera at f = 50 fps and exposure time of t_e = 1/100 s. Adapted from [50].

On the other hand, images like the one in Figure 24b can be used, for example, to estimate the velocity and turbulence level of the jet surface when considering multi-frames. It should be emphasised that in the machine application considered here, it was only possible to measure jet surface velocities. This could be efficiently accomplished by the installed back and front lightning. Therefore, no velocity information could be extracted from the core region of the jets.

The characteristics of the systems studied, and the configurations used by the high-speed camera, are summarised in Table 2.

Table 2. Characteristics of the studied cooling systems and the configurations used by the high-speed camera.

Supply System	Nozzle Diameter	Pressure	Cooling Strategy	Frame Rate	Exposure Time
1	6.5 mm	1.0 bar 2.5 bar	Flood cooling	3600 fps	1/333,000 s
2	5 mm	1.1 bar 2.9 bar	Flood cooling	3600 fps	1/333,000 s
3	top = 2 × 1.2 mm bottom = 1.4 mm	4.7 bar 24.2 bar	High-pressure	30,000 fps	1/1,000,000 s

2.6.1. Evaluation Method (TP11)

Velocity estimation from the jet surface was extracted by standard cross-correlation methods used in PIV analysis available in the open-source software Fiji [51,52]. In order to use this method, it is necessary first to have an image of the jet without the background, as shown in Figure 25a. This image is then converted to binary, and the edges of the jet are extracted. The idea behind extracting the edges is to track them and compare the displacement between successive frames, as illustrated in Figure 25b. This displacement is calculated in numbers of pixels by the cross-correlation method in Fiji, as shown in Figure 25c.

2.6.2. Results and Discussion (TP11)

As mentioned before, the cross-correlation method provides the displacement in pixels for the interrogation area for two subsequent frames. The displacement can be easily converted into velocity by multiplying it by the pixel size and the framerate of the high-speed camera. This analysis of a single pair of images provides the instantaneous velocity of each interrogation area, as shown by the results in Figure 26. The velocities shown in Figure 26a and Figure 26b are for systems 1 and 2, respectively, operated at the lower pump pressure (see Table 2). System 3 is represented by Figure 26c. It is important to highlight that the results in the middle region of the jet are more accurate than on the extremities. This is because the region close to the nozzle outlet does not produce structures protuberant enough to be analysed by the method employed. At the edges of the images, although the

structures can be easily identified, they may disappear from one frame to the other, making it impossible to determine their velocity. It is also noticeable from the results for systems 1 and 2 that the velocity field is quite asymmetric, with the edges on the lower side having higher velocities than those on the top.

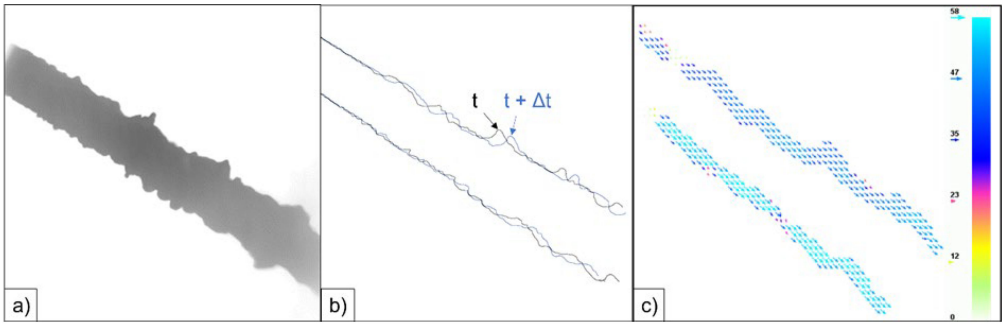

Figure 25. Image enhancement procedure to apply the cross-correlation technique: (**a**) image of the jet without background; (**b**) comparison of the jet edges for two subsequent time steps illustrating how they are tracked; (**c**) raw results (displacement in pixels) of the cross-correlation technique used in PIV.

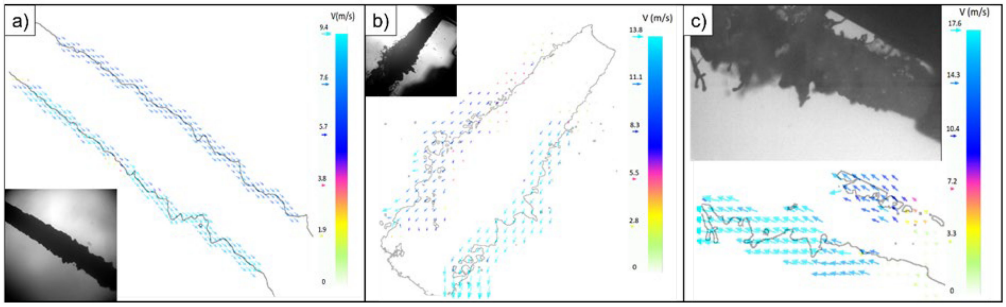

Figure 26. Instantaneous velocities obtained from near the edges of the jets (at low pressure) of (**a**) system 1, (**b**) system 2 and (**c**) the bottom nozzle of system 3. The arrow indicate the flow direction and are coloured according to the flow velocity.

Instantaneous velocity can provide insightful information about the flow, but as the name suggests, it only represents a specific moment in time. Frequently, it is interesting to have results with better statistical information. For that reason, the mean velocities of system 1 are shown in Figure 27a and Figure 27b for lower and higher pressure, respectively. The mean velocities were calculated, in both cases, by averaging the results of the instantaneous velocity fields over 1000 images. The averaged velocities were again obtained from regions near the edges of the jets where interface structures produce sufficient information for the cross-correlation technique to be applied. The lower edges of the jet again showed higher velocities when compared to the upper side, suggesting that the jet inclination may play an important role in the velocity distribution. However, the geometry of the piping system before the jet exit may also cause such an asymmetry. Furthermore, the turbulence level Tu of the jet can be estimated by the ratio between the standard deviation of the fluctuation and the mean velocities [53]. Results for the turbulence level Tu of system 1 are shown in Figure 27c and Figure 27d for lower and higher pressure, respectively. The higher Tu values on the left, close to the nozzle exit, and on the right, close to the edge of the image, are due to the higher inaccuracy of the measurement technique, as already explained above. In addition, the results for the high-pressure pump show a bigger region of enhanced Tu, as expected, since it has higher velocities and, consequently, higher Reynolds number Re.

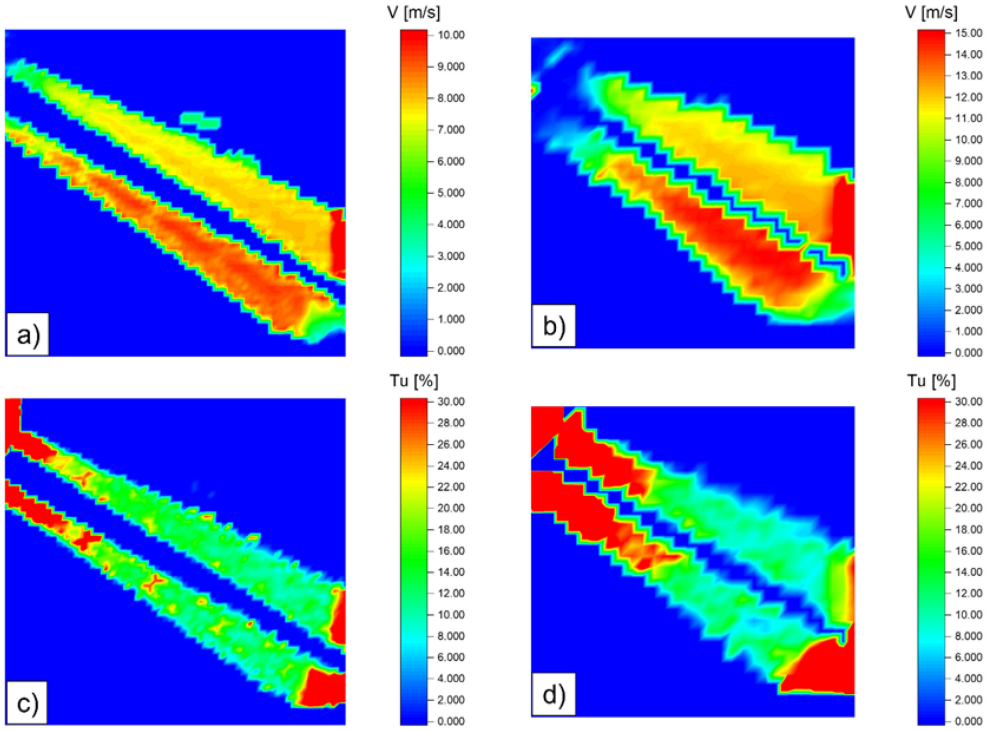

Figure 27. Results obtained by analysing 1000 images of system 1: (**a**) mean velocities for the lower-pressure pump; (**b**) mean velocities for the higher-pressure pump; (**c**) turbulence level for the lower-pressure pump; (**d**) turbulence level for the higher-pressure pump. Adapted from [50].

In order to check the accuracy of the results obtained by the method presented in this work, the average of the mean velocities was used as a constant outlet velocity to calculate the flow rate of each jet. These flow rates were compared with the flow rates obtained by measuring the amount of liquid collected after running each system for a certain duration. The results are summarised in Table 3.

Table 3. Comparison between the results obtained by PIV cross-correlation from Fiji and the bulk flow rate measured in experiments.

Supply System	Pressure (bar)	Flow Rate CC (L/min)	Flow Rate Bulk (L/min)	Error (%)
1	1	15.15	15.43	−1.81
	2.5	21.36	24.35	−12.28
2	1.1	10.79	13.69	−21.18
	2.9	15.99	21.65	−26.14
3	4.7	3.35	3.15	6.35
	24.2	6.01	6.75	−10.96

The results obtained by the cross-correlation (CC) were closer to the measured bulk flow rate for all systems with lower pressure. This may be due to the smaller displacement between frames due to the reduced velocities. Bigger displacements between frames can potentially lead to errors or difficulties in tracking the structures [54]. It is also important to highlight that system 2 had very large oscillations in the jet. These oscillations were probably caused by the nozzle geometry and possible flow separations inside the screw-like nozzle, which made the jet expand and contract very frequently. This may also be the main reason for the higher errors associated with system 2 (Table 3).

2.6.3. Conclusion (TP11)

A methodology for measuring the velocity distribution over the edges of cooling liquid-free jets was presented. The method consists of using high-speed imaging to record the jet and then track its edges from one frame to the other in order to determine the displacement. The instantaneous velocity can be obtained by multiplying the displacement (in pixels) by the framerate and the pixel size. A more statistical analysis is feasible by analysing several images, which provide the mean velocity and turbulence distribution over the jet edges. Three different cooling systems were analysed, with system 2 showing the biggest differences for the flow rate estimation, when compared to the bulk flow rate. This difference is assumed to be due to the internal shape of the nozzle, which caused large oscillations in the jet, making it frequently expand and contract.

2.7. Electrochemical Machining with Superimposed Magnetic Field—MPECM (SPP 2231-TP12)

The ongoing enhancement and optimisation of technological processes lead to constantly rising requirements regarding the utilised components in terms of complexity and functionality. This trend directly transfers to the involved manufacturing processes. One technique that shows great potential for meeting these growing demands is electrochemical machining (ECM). This procedure is based on anodic metal dissolution due to the application of a voltage between the workpiece (anode) and the tool (cathode) with electrolytes between them, ensuring electrical conductivity between both parts. Recent studies indicate that the removal process can be particularly effective when the machining zone is superimposed with an external magnetic field. Higher machining rates with lower surface roughness [55–57] and better localisation of the processing due to reduced abrasions outside the main process zone [58] have been reported. Furthermore, the magnetic field superimposition significantly impacts the electrolyte flow, especially around surface structures of the electrodes [59,60]. Hence, understanding the underlying mechanisms in order to specifically adjust process parameters to overcome the present limits of the manufacturing technique is a topic of great interest for research and industry. Therefore, the goal of this work was to investigate the effects of the superimposed magnetic field on the ECM process and the related electrolyte flow using optical measurement techniques such as particle image velocimetry (PIV) and shadowgraphy. The following subsections provide an overview of the experimental setup and methods used and show some flow visualisation results.

2.7.1. Experimental Setup (MPECM-TP12)

In typical ECM processes, electric current density values up to J = 100 A/cm^2 are used with working gap distances L, i.e., the distances between the electrodes (workpiece and tool), ranging from 50 to 200 µm [61]. The latter strongly limits the accessibility of optical measurement techniques such as PIV and shadowgraphy. To be able to investigate the resulting electrolyte flow in situ between the electrodes, an analysis cell with upscaled dimensions was built that meets a working gap distance of L = 10 mm. To ensure comparability between process parameters and conditions used for the up-scaled cell and in typical ECM processes, dimensionless numbers were introduced. This procedure is described in more detail by Luther et al. [62]. The cell consists of a main body made from polyoxymethylene with acrylic windows on four sides granting optical access and additional rectangular openings on the top and bottom sides. The latter are used to install stainless steel pockets capable of incorporating permanent magnets (NdFeB N45, average magnetic flux density on the surface: 0.25 T) for the application of an external magnetic field and are closed with exchangeable electrodes (material: paramagnetic aluminium alloy AW-5083) which serve as lids to the pockets. This design enables a flexible approach for fast adaptions of the working gap distance and the magnetic field intensity, also allowing an easy replacement of worn-out electrodes. To apply an external voltage and ensure stable process conditions, a constant current source (EA-PSI 5080-20 A, EA-Elektro-Automatik GmbH, Viersen, Germany) is connected to both pockets and the attached electrodes. For

flushing the analysis cell and especially the working gap with electrolytes (aqueous solution with 9.5 wt. % sodium nitrate; ρ = 1052.5 kg/m^3 and η = 10.42 $\times$ 10^{-4} Pa·s), a peristaltic pump (Perimax 16—Antipuls, Spetec GmbH, Erding, Germany) is utilised that provides an almost pulse-free and adjustable flow. To visualise the flow, hollow glass spheres (particle diameter from 8 µm to 12 µm; particle density from 1050 kg/m^3 to 1150 kg/m^3) are added as tracer particles to the utilised electrolyte. They are illuminated using a Nd:YAG laser (nano L PIV, Litron Lasers, Rugby, England) that casts a thin light sheet through the side windows of the measuring cell. To track the motion of the particles, two CCD cameras with Scheimpflug adapters (VC-Imager CX-5, LaVision GmbH, Göttingen, Germany) and lenses (AF Nikkor 50 mm 1:1.8D, Nikon, Tokyo, Japan) are located on both sides of the cell, facing towards the light source. This way, the observed image intensities are equal for both cameras. The presented setup enables 2D3C stereo PIV measurements, i.e., the determination of three-dimensional velocity components in a two-dimensional measurement plane. The setup is shown in Figure 28.

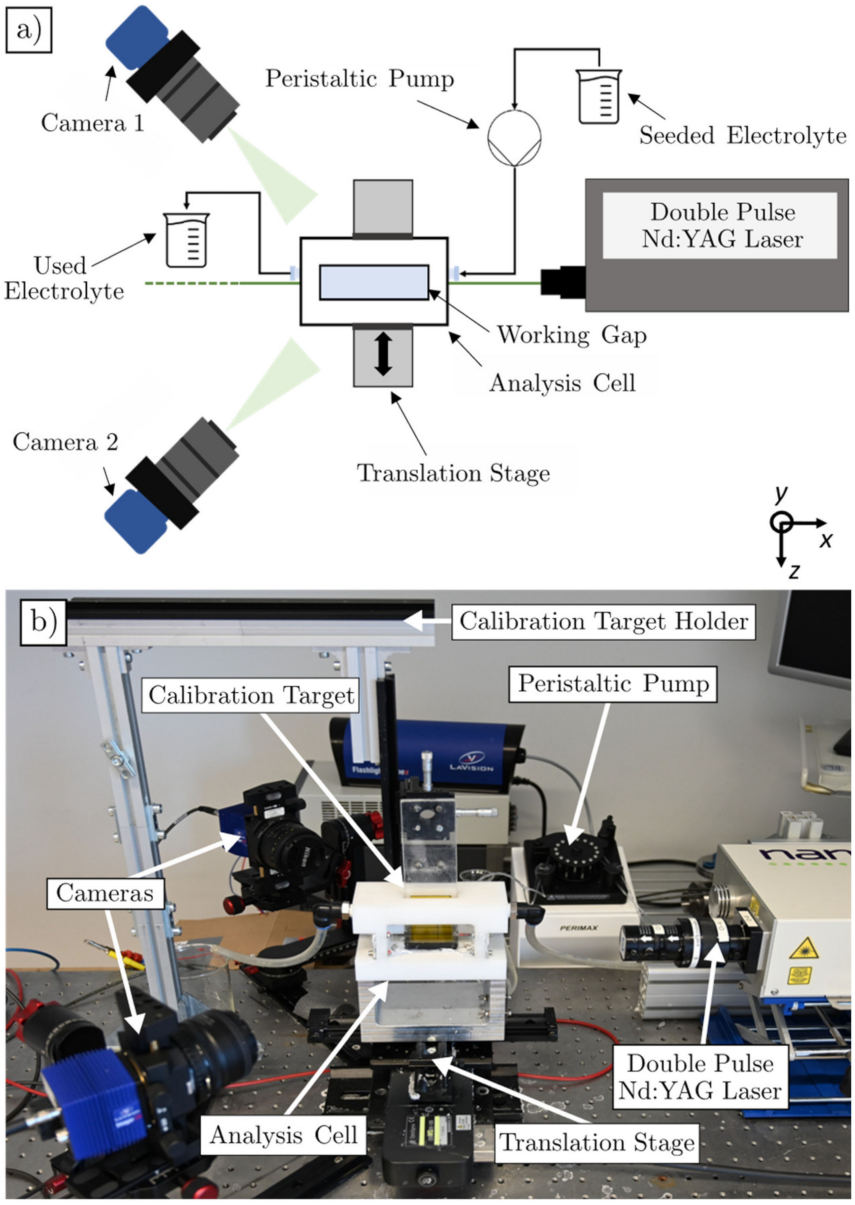

Figure 28. (**a**) Schematic overview of the experimental PIV setup and (**b**) photograph of the experimental setup in the calibration phase, i.e., with calibration target holder and calibration target within the analysis cell.

2.7.2. Data Analysis and Post-Processing (MPECM-TP12)

A reliable calibration must be carried out prior to the actual investigations to enable accurate measurements. The best results are usually obtained with in situ calibrations to ensure consistent optical conditions between the calibration and the experiment. For this, the upper magnet pocket can be temporarily removed to insert a calibration target directly into the analysis cell filled with electrolytes (see Figure 29a). Typically, a 3D calibration target with two levels is utilised in stereo PIV applications. However, due to the limited size of the working gap, a micro 2D plane calibration target (LaVision GmbH, Göttingen, Germany; point diameter: 0.15 mm, point distance: 0.5 mm) was used instead. The target was attached to a holder placed on a micro-translation stage, allowing a precise positioning of the target within the laser plane. Additionally, the analysis cell was installed on a controllable micro-translation stage (see Figure 28b). To calibrate the out-of-plane component with the plane target, two calibration positions were necessary. In the first position, the calibration target was aligned with the laser in the middle of the analysis cell. For the second position, the analysis cell was moved 1 mm while the rest of the setup remained fixed. A close-up of the calibration target within the working gap is shown in Figure 29.

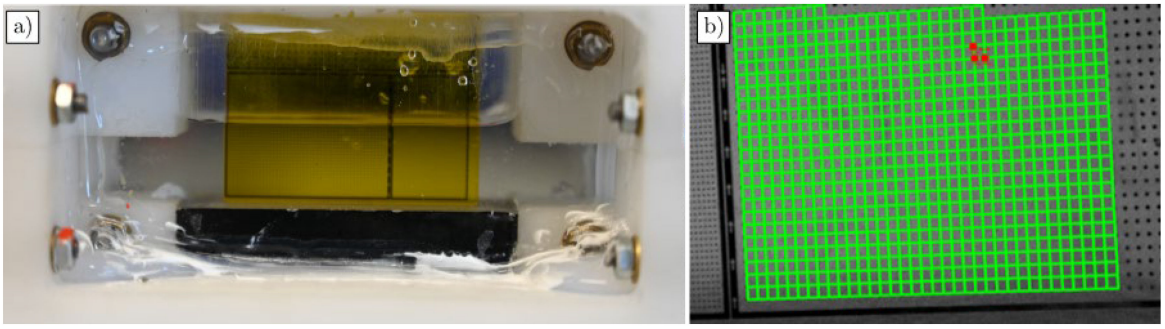

Figure 29. (**a**) Image of the calibration target within the working gap filled with electrolyte for in situ calibration and (**b**) image of a successful calibration within DaVis.

The images were recorded and evaluated using the software DaVis 10.2.1 FlowMaster (LaVision GmbH, Göttingen, Germany). The flow field calculation was carried out in multipass mode. Hereby, for the first evaluation stage, the image was subdivided into 64 × 64-pixel interrogation windows with 50% overlap and into 32 × 32-pixel windows with 75% overlap for the second stage. In order to further increase the quality of the data, self-calibration in the DaVis software was used. This tool accounts for slight misalignments between the laser plane and the calibration target, based on disparity vectors of individual particles between the recorded images of both cameras and corrects them [63]. The recording rate of the cameras was adapted to a maximum observed pixel shift in individual particles of around 30% within a 32 × 32-pixel interrogation window between two subsequent images. For most measurements, 15 Hz was suitable, corresponding to an examined process time of about 6.5 s for a total number of 100 recorded images. To obtain the final results of the PIV measurements, 45 subsequent images were averaged.

2.7.3. Results and Discussion (MPECM-TP12)

One of the major issues while conducting the PIV measurements was the heavy gas formation at the electrodes due to the occurring electrochemical reactions. The amount of emerging gas strongly depends on the process parameters, especially the electric current density. Uprising bubbles within the working gap usually have larger diameters than most of the tracer particles. Thus, when illuminated in the laser plane, they can easily be misidentified as particles and corrupt the measurements with false vectors due to their flow-independent behaviour. Additionally, gas bubbles locally lead to an absence of actual tracer particles, resulting in non-evaluable areas within the image. This effect can be minimised

by averaging over several images as the bubble location changes between them. However, with increasing processing time, more and more bubbles accumulate, especially at the electrode surfaces, decreasing the image quality, and also impacting the image intensities. One approach to reducing these negative impacts of the bubbles is to use rhodamine-dotted particles with suitable bandwidth filters in front of the cameras. This way, only the actual tracer particles are illuminated within the images, thus strongly increasing the quality of the recordings and the consistency throughout the measurements over time. This behaviour is illustrated in Figure 30.

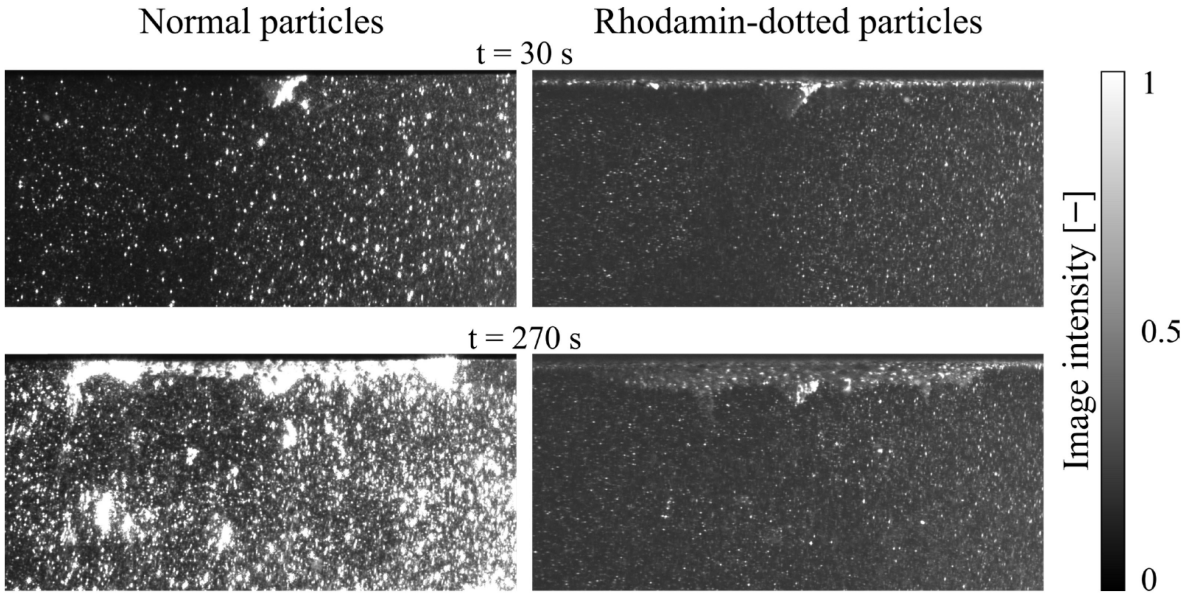

Figure 30. Recorded images within the working gap after a 30 s and 270 s process time using normal particles (**left**) and rhodamine-dotted particles (**right**), respectively.

In the following, a few exemplary results of the PIV measurements within the working gap are shown. The process parameters were set to an electric current density of $J = 0.012$ A/cm^2 and a magnetic field density of $B = 100$ mT. Instead of a full metallic electrode, an acrylic glass plate with a circular aluminium insert with a diameter of 10 mm was used for the experiments (electrode position is highlighted in Figure 31). Figure 31 shows the observed flow fields for a simple ECM process, i.e., just the electrical current without electrolyte flushing (case 1, left side) and an ECM process with the same conditions but with a superimposed magnetic field (case 2, right side). One significant difference between both processes is the resulting mean velocity. Due to the present electromagnetic forces in case 2, the flow is strongly accelerated. This can lead to a faster transport of reaction products and emerging gas bubbles that might inhibit the reaction from the process zone, thus potentially increasing the stability of the process conditions. Although all observed velocity components in case 1 are negligibly small compared to the velocities in case 2, the highest velocities for the ECM process without magnetic field assistance occur in positive v direction with almost zero velocity in all other directions (see vectors in the average plot of Figure 31). This is mainly due to the charge transport between the electrodes and the emerging gas bubbles in this direction. For case 2, however, the highest velocities occur in the out-of-plane w direction, with positive values on the right side and negative values on the left side of the working gap. This behaviour indicates a vortex formation around the electrodes due to electromagnetic forces.

To evaluate the three-dimensional flow field not only within the laser plane (2D3C) but within a larger volume of the cell (3D3C), a quasi-tomographic approach was introduced. This method uses the controllable translation stage to move the position of the analysis cell while the laser and camera positions are fixed to maintain the focus and calibration on the laser plane. Subsequent stereo PIV measurements at different z positions form the basis for

reconstructing the three-dimensional flow from the individual measurements. Because the flow structures in the conducted experiments appear rather stable, the time discrepancies between the recordings are negligible and do not affect the qualitative behaviour of the results. Figure 32 shows the quasi-tomographic approach schematically and provides the evaluated flow field in the x–z direction of an exemplary plane of interest for case 2. These results can provide further information about the flow behaviour and the effects of certain process parameters. In these experiments, they validate that due to the magnetic field, a vortex structure forms locally around the electrodes.

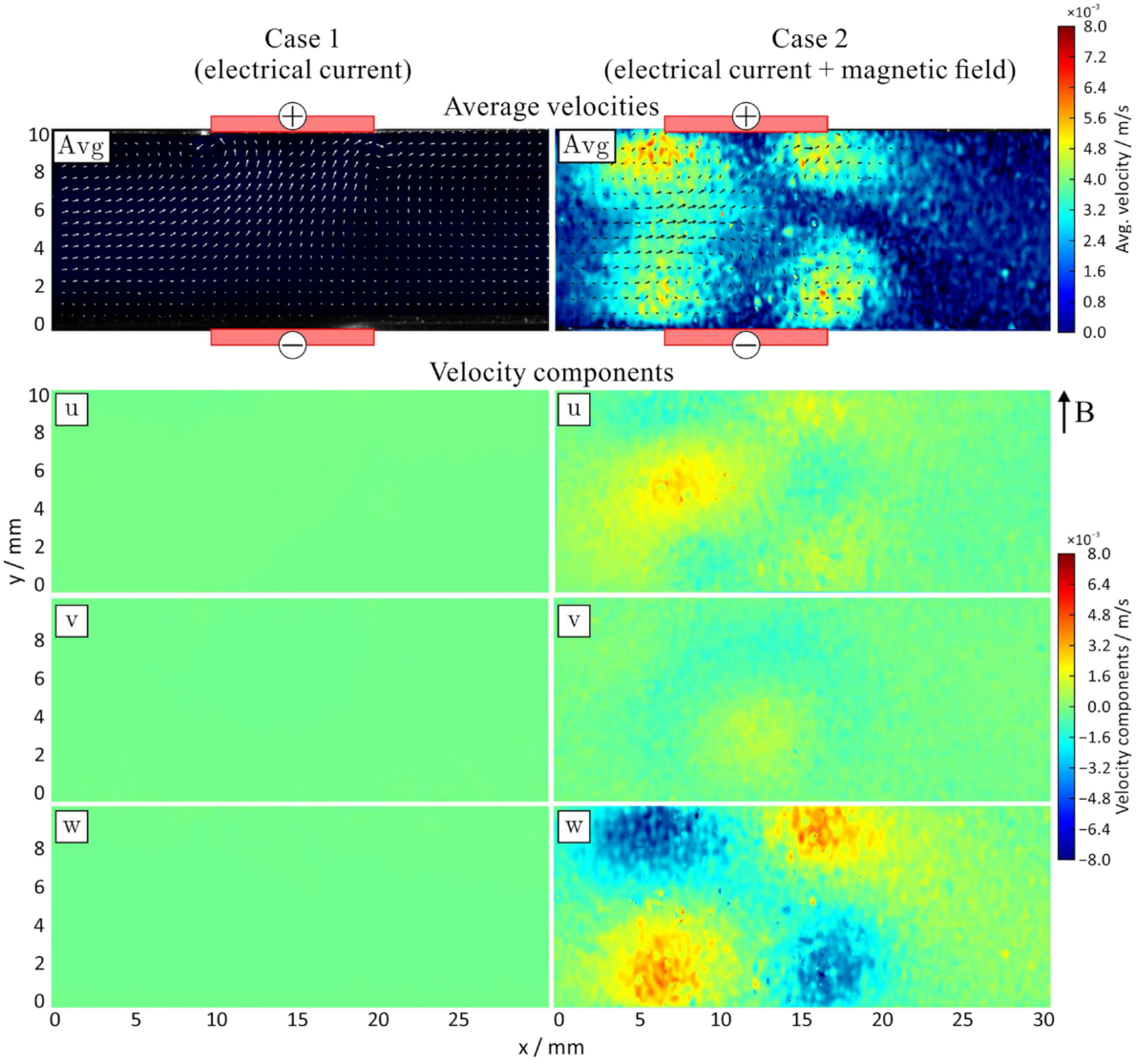

Figure 31. Flow fields within the working gap for a simple ECM process (only electric current; case 1, left side) and an ECM process with magnetic field assistance (case 2, right side). Shown are the average velocities with vectors indicating the present flow in the x–y direction and the individual velocity components in the x (u), y (v), and z (w) directions. The red boxes indicate the positions of the circular aluminium electrodes within the acrylic glass plates.

In further work, the impact of several process parameters, e.g., electric current density, magnetic field density, and volume flow rate, will be further investigated not only for flat electrode surfaces but also for functionalised structures like upscaled roughness peaks. Furthermore, shadowgraphy will be applied to track the emerging reaction gas bubbles to indicate the process conditions and speed. Ultimately, these results will be

used to characterise the process behaviour based on the process parameters and validate simulation models.

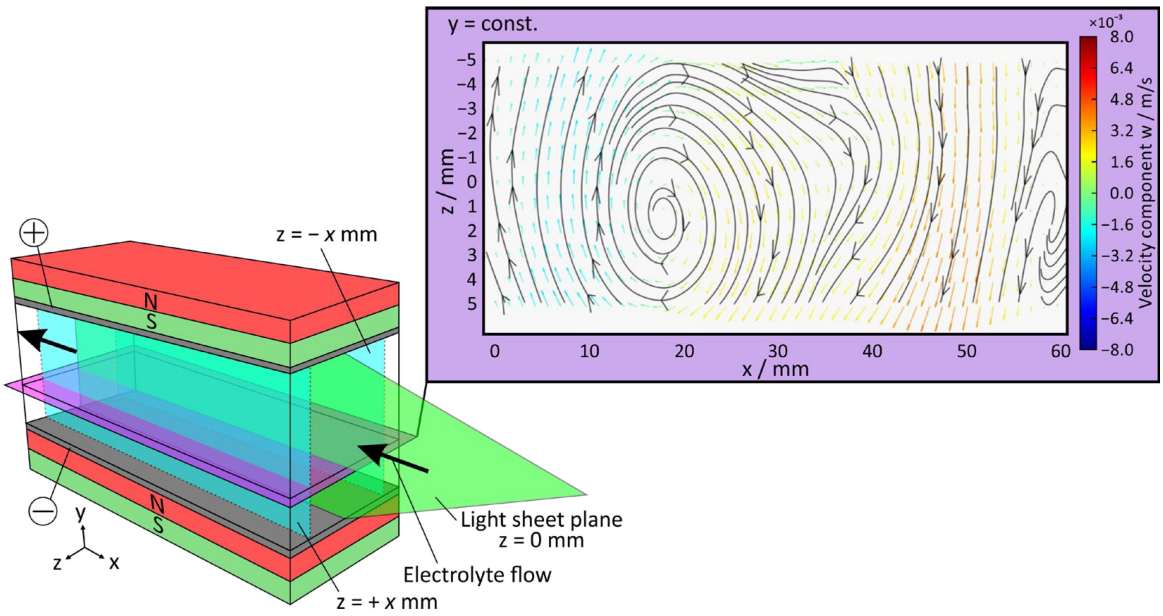

Figure 32. Schematic drawing of the quasi-tomographic measurement approach with a rectangular plane electrode (right side) to determine the three-dimensional flow behaviour within the analysis cell using complementary x–y plane measurements at different z positions. Streamlines are used to highlight the resulting flow directions.

3. Conclusions

In the SPP FluSimPro, intensive collaborative research is carried out to optimise the use of metalworking fluids in metal manufacturing processes. The combination of experimental analysis and numerical simulation is used to determine effective machine operating parameters and efficient use of metalworking fluids. Recent investigations suffer from the difficulty of approaching the MWF application zone and directly observing the complex fluid–structure interactions in the manufacturing process. In this context, experimental MWF flow analysis is performed using several approaches within flow visualisation and evaluation studies in manufacturing processes.

The paper describes flow visualisation and flow analysis studies, the specific methods, and results in different machining processes:

- Ejector deep hole drilling: PIV was shown to be an efficient and valid analysis tool, allowing quantitative and qualitative comparisons and evaluations of the flow characteristics in the tool system in the experimentally recorded MWF flow.
- Discontinuous drilling: By comparing the flow simulation with high-speed PTV experiments, a qualified method is established to validate the numerical work and to optimise the heat transfer from the highly loaded cutting edges to the fluid in parallel with the process analysis.
- Vibration-assisted drilling: Shadowgraphy proved capable of distinguishing different flow regimes and generating a regime map to characterise the MQL flow behaviour as a function of the operating conditions of air and MWF input pressures.
- Circular saw with internal coolant supply: Two test setups showed that an internal coolant supply has a significant effect on the curling of the chip formation process and that a 0° inflow angle appears to be the best in terms of cost–benefit assessment.
- Precise electrochemical machining: An analogue test rig for observing gas transport showed that regions with high concentrations of gas bubbles had lower velocities and that these gas bubbles tended to coalesce.

- Flood and jet cooling machining: A method for measuring the velocity distribution over the edges of coolant-free jets was presented, consisting of high-speed imaging to record the jet and edge tracking.
- Superimposed magnetic field electrochemical machining: A quasi-tomographic approach was presented using stereo PIV measurements to reconstruct the three-dimensional flow from the individual measurements.

Valuable insights were gained into machining operations that are difficult to access directly in the machine. A series of generic experimental setups and model experiments were set up to access the machining zone. Shadowgraph imaging and flow measurements, such as particle image velocimetry, have been used to identify typical flow regimes in the various machining processes. Based on these regimes, efficient machining parameters and MWF applications have been derived.

The experimental analysis of MWFs also provides essential data for input and validation of numerical simulations within the SPP FluSimPro. Future investigations within the SPP FluSimPro will focus on tool and process optimisation. This will require validated integrated process models that couple tool and workpiece behaviour with the MWF application. Computational time-reduced MWF flow simulations with result-oriented manufacturing optimisations as well as the implementation and validation of innovative FEM-CFD strategies for 3D simulations will be derived.

Author Contributions: Conceptualization, A.K., A.S., B.K., C.M., D.B., E.T., F.L., H.-C.M., I.S, J.F.G., J.S., K.A., K.N., L.B., L.H., L.S., M.R., M.S., T.H., T.T., T.W. and U.F.; methodology, A.K., A.S., B.K., C.M., D.B., E.T., F.L., H.-C.M., I.S., J.F.G., J.S., K.A., K.N., L.B., L.H., L.S., M.R., M.S., T.H., T.T., T.W. and U.F.; software, C.M., E.T., F.L., I.S., J.F.G., J.G., J.S., K.A., K.N., L.B., L.H., L.S., T.T. and T.W.; validation, C.M., E.T., F.L., I.S., J.D.H., J.F.G., J.G., J.S., K.A., K.N., L.B., L.H., L.S., T.T. and T.W.; formal analysis, C.M., E.T., F.L., I.S., J.F.G., J.S., K.A., K.N., L.B., L.H., L.S., T.T. and T.W.; investigation, C.M., E.T., F.L., I.S., J.D.H., J.F.G., J.G., K.N., L.B., L.H., L.S., T.T. and T.W.; resources, A.K., A.S., B.K., D.B., H.-C.M., J.S., K.A., M.R., M.S., T.H. and U.F.; data curation, C.M., E.T., F.L., I.S., J.F.G., K.N., L.S., T.T. and T.W.; writing—original draft preparation, A.K., A.S., B.K., C.M., D.B., E.T., F.L., H.-C.M., I.S., J.F.G., J.S., K.A., K.N., L.B., L.H., L.S., M.R., M.S., T.H., T.T., T.W. and U.F.; writing—review and editing, A.K., A.S., B.K., C.M., D.B., E.T., F.L., H.-C.M., I.S., J.F.G., J.S., K.A., K.N., L.B., L.H., L.S., M.R., M.S., T.H., T.T., T.W. and U.F.; visualization, C.M., E.T., F.L., I.S., J.F.G., K.N., L.B., L.H., L.S., T.T., T.W. and U.F.; supervision, A.K., A.S., B.K., D.B., H.-C.M., M.R., M.S. and U.F.; project administration, A.K., A.S., B.K., D.B., H.-C.M., M.R., M.S. and U.F.; funding acquisition, A.K., A.S., B.K., D.B., H.-C.M., M.R., M.S. and U.F. All authors have read and agreed to the published version of the manuscript.

Funding: This research was funded by the German Research Foundation (Deutsche Forschungsgemeinschaft DFG) within the SPP FluSimPro under grant number 422633203 and the individual TP projects under grant numbers TP03: 439917965; TP04: 439920593; TP08: 439950037; TP09: 439925537; TP10: 439915866; TP11: 439626733; and TP12: 439920154.

Conflicts of Interest: The authors declare no conflict of interest. The funders had no role in the design of the study; in the collection, analyses, or interpretation of data; in the writing of the manuscript; or in the decision to publish the results.

References

1. FluSimPro SPP 2231. Available online: https://flusimpro.isf.maschinenbau.tu-dortmund.de/projekte/ (accessed on 3 July 2023).
2. Leiden, A.; Arafat, R.; Callegari, M.; Kolb, M.; Herrmann, C.; Wichmann, H. Development and testing of novel mineral oil- and biocide-free glycerol- and propanediol-based fluids for drilling and tapping aluminium alloys. *Int. J. Adv. Manuf. Technol.* **2023**, *126*, 2323–2336. [CrossRef]
3. Rashmi, W.; Osama, M.; Khalid, M.; Rasheed, A.K.; Bhaumik, S.; Wong, W.Y.; Datta, S.; Tcsm, G. Tribological performance of nanographite-based metalworking fluid and parametric investigation using artificial neural network. *Int. J. Adv. Manuf. Technol.* **2019**, *104*, 359–374. [CrossRef]
4. Klocke, F.; König, W. *Fertigungsverfahren 1—Drehen, Fräsen, Bohren*, 8th ed.; Springer: Berlin/Heidelberg, Germany, 2008.
5. Eltaggaz, A.; Pervaiz, S. (Eds.) *Minimum Quantity Lubrication: Environmental Alternatives in Processing*; Special Issue: *Lubricants*; MDPI: Basel, Switzerland, 2023.
6. Brinksmeier, E.; Meyer, D.; Huesmann-Cordes, A.G.; Herrmann, C. Metalworking fluids—Mechanisms and performance. *CIRP Ann.* **2015**, *64*, 605–628. [CrossRef]

7. Weinert, K.; Inasaki, I.; Sutherland, J.W.; Wakabayashi, T. Dry Machining and Minimum Quantity Lubrication. *CIRP Ann.* **2004**, *53*, 511–537. [CrossRef]
8. Dasch, J.M.; Kurgin, S.K. A characterisation of mist generated from minimum quantity lubrication (MQL) compared to wet machining. *Int. J. Mach. Mach. Mater.* **2010**, *7*, 82–95. [CrossRef]
9. Tai, B.L.; Stephenson, D.A.; Furness, R.J.; Shih, A.J. Minimum Quantity Lubrication (MQL) in Automotive Powertrain Machining. *Procedia CIRP* **2014**, *14*, 523–528. [CrossRef]
10. Jawahir, I.S.; Attia, H.; Biermann, D.; Duflou, J.; Klocke, F.; Meyer, D.; Newman, S.T.; Pusavec, F.; Putz, M.; Rech, J.; et al. Cryogenic manufacturing processes. *CIRP Ann.* **2016**, *65*, 713–736. [CrossRef]
11. Khanna, N.; Agrawal, C.; Pimenov, D.Y.; Singla, A.K.; Machado, A.R.; da Silva, L.R.R.; Gupta, M.K.; Sarikaya, M.; Krolczyk, G.M. Review on design and development of cryogenic machining setups for heat resistant alloys and composites. *J. Manuf. Process.* **2021**, *68*, 398–422. [CrossRef]
12. Daniel, D.M.; Moraes, D.L.d.; Garcia, M.V.; Lopes, J.C.; Rodriguez, R.L.; Ribeiro, F.S.F.; Sanchez, L.E.d.A.; Bianchi, E.C. Application of MQL with cooled air and wheel cleaning jet for greener grinding process. *Int. J. Adv. Manuf. Technol.* **2022**, *125*, 435–452. [CrossRef]
13. Maruda, R.W.; Krolczyk, G.M.; Feldshtein, E.; Pusavec, F.; Szydlowski, M.; Legutko, S.; Sobczak-Kupiec, A. A study on droplets sizes, their distribution and heat exchange for minimum quantity cooling lubrication (MQCL). *Int. J. Mach. Tools Manuf.* **2016**, *100*, 81–92. [CrossRef]
14. Rahim, E.A.; Dorairaju, H. Evaluation of mist flow characteristic and performance in Minimum Quantity Lubrication (MQL) machining. *Measurement* **2018**, *123*, 213–225. [CrossRef]
15. Raval, J.K.; Hung, W.N.P.; Tai, B.L. Multiphase Flow Distribution in MQL Drilling Using Optical Intensity Distribution Based Approach. In Proceedings of the ASME 2019 14th International Manufacturing Science and Engineering Conference, Erie, PA, USA, 10–14 June 2019. [CrossRef]
16. Meyer, D.; Schumski, L.; Guba, N.; Espenhahn, B.; Hüsemann, T. Relevance of the region of interaction between the tool and the metalworking fluid for the cooling effect in grinding. *CIRP Ann.* **2022**, *71*, 301–304. [CrossRef]
17. Buss, L.; Schumski, L.; Sölter, J.; Avila, K.; Karpuschewski, B.; Fritsching, U. Minimum Quantity Lubrication (MQL) multiphase dynamics of a vibration-assisted drilling process. *Procedia CIRP* **2023**, *117*, 420–425. [CrossRef]
18. Raval, J.K.; Tai, B.L. Mist Flow in Through-Tool Minimum Quantity Lubrication Drilling: Two-Phase Flow Simulation and Experimental Observation. *J. Manuf. Sci. Eng.* **2023**, *145*, 031002. [CrossRef]
19. Biermann, D.; Bleicher, F.; Heisel, U.; Klocke, F.; Möhring, H.C.; Shih, A. Deep hole drilling. *CIRP Ann.* **2018**, *67*, 673–694. [CrossRef]
20. Astakhov, V.P. *Drills: Science and Technology of Advanced Operations*, 1st ed.; CRC Press: Boca Raton, FL, USA, 2014.
21. Gerken, J.F.; Canini, D.; Biermann, D.; Eberhard, P. Analysis of the cooling lubricant flow in the area of cutting edges and guide pads during ejector deep hole drilling. *Procedia CIRP* **2023**, *117*, 408–413. [CrossRef]
22. Wolf, T.; Iovkov, I.; Biermann, D. Discontinuous Drilling of Inconel 718. *MM Sci. J.* **2021**, *2021*, 4569–4575. [CrossRef]
23. Wolf, T.; Iovkov, I.; Biermann, D. Influence of a Discontinuous Process Strategy on Microstructure and Microhardness in Drilling Inconel 718. *J. Manuf. Mater. Process.* **2021**, *5*, 43. [CrossRef]
24. Fast, M.; Mierka, O.; Turek, S.; Wolf, T.; Biermann, D. Mathematical Modeling of Coolant Flow in Discontinuous Drilling Processes with Temperature Coupling. *Proc. Appl. Math. Mech.* **2023**, *22*, e202200142. [CrossRef]
25. Oezkaya, E.; Michel, S.; Biermann, D. Experimental and computational analysis of the coolant distribution considering the viscosity of the cutting fluid during machining with helical deep hole drills. *Adv. Manuf.* **2022**, *10*, 235–249. [CrossRef]
26. Heyman, J. TracTrac: A fast multi-object tracking algorithm for motion estimation. *Comput. Geosci.* **2019**, *128*, 11–18. [CrossRef]
27. Sadek, A.; Aly, M.; Hamza, K.; Meshreki, M.; Nassef, A.O.; Attia, H. Optimization of Cutting Conditions in Vibration Assisted Drilling of Composites via a Multi-Objective EGO Implementation. In Proceedings of the ASME 2015 International Design Engineering Technical Conferences and Computers and Information in Engineering Conference, Boston, MA, USA, 2–5 August 2015. [CrossRef]
28. Bleicher, F.; Wiesinger, G.; Kumpf, C.; Finkeldei, D.; Baumann, C.; Lechner, C. Vibration assisted drilling of CFRP/metal stacks at low frequencies and high amplitudes. *Prod. Eng.* **2018**, *12*, 289–296. [CrossRef]
29. Paulsen, T.; Guba, N.; Sölter, J.; Karpuschewski, B. Influence of the workpiece material on the cutting performance in low frequency vibration assisted drilling. *CIRP J. Manuf. Sci. Technol.* **2020**, *31*, 140–152. [CrossRef]
30. Osman, K.A.; Ünver, H.Ö.; Şeker, U. Application of minimum quantity lubrication techniques in machining process of titanium alloy for sustainability: A review. *Int. J. Adv. Manuf. Technol.* **2018**, *100*, 2311–2332. [CrossRef]
31. He, T.; Liu, N.; Xia, H.; Wu, L.; Zhang, Y.; Li, D.; Chen, Y. Progress and trend of minimum quantity lubrication (MQL): A comprehensive review. *J. Clean. Prod.* **2023**, *386*, 135809. [CrossRef]
32. Pecat, O. Vibrationsunterstütztes Bohren von Werkstoffverbunden aus CFK und Titan. Ph.D. Thesis, University of Bremen, Bremen, Germany, 2018.
33. Stampfer, B.; Zanger, F.; Schulze, V. In-Process Analysis of Minimum Quantity Lubrication during Drilling of AISI 4140. In *Advances in Production Research, Proceedings of the WPG 2018, Aachen, Germany, 19–20 November*; Schmitt, R., Schuh, G., Eds.; Springer: Cham, Switzerlad, 2019; pp. 541–550. [CrossRef]
34. Möhring, H.-C.; Menze, C.; Werkle, K.T. Internal coolant supply in circular sawing. *CIRP Ann.* **2023**, *72*, 353–356. [CrossRef]

35. Fang, Z.; Obikawa, T. Influence of cutting fluid flow on tool wear in high-pressure coolant turning using a novel internally cooled insert. *J. Manuf. Processes* **2020**, *56*, 1114–1125. [CrossRef]
36. Lakner, T.; Bergs, T.; Döbbeler, B. Additively manufactured milling tool with focused cutting fluid supply. *Procedia CIRP* **2019**, *81*, 464–469. [CrossRef]
37. Tismer, A.; Menze, C.; Straub, P.; Stegmann, J.; Riedelbauch, S.; Möhring, H.-C.; Kabelac, S. Simulation-based evaluation of the 3D fluid dynamics of a coolant lubricant in the narrow-closed cutting gap during circular sawing. *Procedia CIRP* **2023**, *117*, 402–407. [CrossRef]
38. McGeough, J.A. *Principles of Electrochemical Machining*; Chapman and Hall: London, UK, 1974.
39. Rajurkar, K.P.; Kozak, J.; Wei, B.; McGeough, J.A. Study of Pulse Electrochemical Machining Characteristics. *CIRP Ann.* **1993**, *42*, 231–234. [CrossRef]
40. Reed, R.C. *The Superalloys*; Cambridge University Press: Cambridge, UK, 2006.
41. Ernst, A.; Heib, T.; Hall, T.; Schmidt, G.; Bähre, D. Simulation of the Tool Shape Design for the Electrochemical Machining of Jet Engine Vanes. *Procedia CIRP* **2018**, *68*, 762–767. [CrossRef]
42. Rajurkar, K.P.; Zhu, D.; McGeough, J.A.; Kozak, J.; De Silva, A. New Developments in Electro-Chemical Machining. *CIRP Ann.* **1999**, *48*, 567–579. [CrossRef]
43. Ernst, A. Analyse und Modellierung der Einflüsse auf das Arbeitsergebnis der Elektrochemischen Bearbeitung Hochtemperaturfester Werkstoffe für Turbinenstrahltriebwerke. Ph.D. Thesis, Saarland University, Saarbrücken, Germany, 2020. [CrossRef]
44. Tchoupe, E.; Lauwers, D.; Heidemanns, L.; Herrig, T.; Klink, A.; Meinke, M.; Klaas, M.; Schröder, W. Optical in Situ Analysis of Gas Bubble Evolution in Electrochemical Machining Based on Similarity Theory Using Particle Image Velocimetry. *Procedia CIRP* **2023**, *117*, 257–262. [CrossRef]
45. Rommes, B.; Lauwers, D.; Herrig, T.; Meinke, M.; Schrder, W.; Klink, A. Concept for the experimental and numerical study of fluid-structure interaction and gas transport in Precise Electrochemical Machining. *Procedia CIRP* **2021**, *102*, 204–209. [CrossRef]
46. Raffel, M.; Willert, C.E.; Scarano, F.; Kähler, C.J.; Wereley, S.T.; Kompenhans, J. *Particle Image Velocimetry: A Practical Guide*, 3rd ed.; Springer: Cham, Switzerland, 2018; p. 668.
47. Klocke, F.; Zeis, M.; Herrig, T.; Harst, S.; Klink, A. Optical in Situ Measurements and Interdisciplinary Modeling of the Electrochemical Sinking Process of Inconel 718. *Procedia CIRP* **2014**, *24*, 114–119. [CrossRef]
48. Tchoupe, E.; Heidemanns, L.F.; Herrig, T.; Klink, A.; Lauwers, D.; Schöder, W. Study of the multiphase electrolyte flow during electrochemical machining (ECM) using dynamic similarity. In Proceedings of the 17th International Symposium on Electrochemical Machining Technology INSECT 2021, Leuven, Belgium, 25–26 November 2021; pp. 15–21.
49. Versluis, M. High-speed imaging in fluids. *Exp. Fluids* **2013**, *54*, 1–35. [CrossRef]
50. Uhlmann, E.; Barth, E.; Nabbout, K.; Sommerfeld, M.; Bock-Marbach, B.; Kuhnert, J.; Dovgal, A. Cooling Lubricant Boundary Conditions for wet Turning Simulations. *Procedia CIRP* **2023**, *118*, 384–389. [CrossRef]
51. Schindelin, J.; Arganda-Carreras, I.; Frise, E.; Kaynig, V.; Longair, M.; Pietzsch, T.; Preibisch, S.; Rueden, C.; Saalfeld, S.; Schmid, B.; et al. Fiji: An open-source platform for biological-image analysis. *Nat. Methods* **2012**, *9*, 676–682. [CrossRef]
52. Tseng, Q.; Duchemin-Pelletier, E.; Deshiere, A.; Balland, M.; Guillou, H.; Filhol, O.; Théry, M. Spatial organization of the extracellular matrix regulates cell–cell junction positioning. *Proc. Natl. Acad. Sci. USA* **2012**, *109*, 1506–1511. [CrossRef]
53. Scharnowski, S.; Bross, M.; Kähler, C.J. Accurate turbulence level estimations using PIV/PTV. *Exp. Fluids* **2018**, *60*, 1. [CrossRef]
54. Raffel, M.; Willert, C.E.; Kompenhans, J. *Particle Image Velocimetry: A Practical Guide*; Springer: Berlin, Germany, 1998; p. 255.
55. Bradley, C. Anodic Dissolution Model Parameterization for Magnetically-Assisted Pulsed Electrochemical Machining (PECM). In Proceedings of the 2018 COMSOL Conference, Boston, MA, USA, 3–5 October 2018.
56. Bradley, C.; Samuel, J. MHD Electrolyte Flow within an Inter-electrode Gap Driven by a Sinusoidal Electric Field and Constant Magnetic Field. In Proceedings of the 2017 COMSOL Conference, Boston, MA, USA, 4–6 October 2017.
57. Bradley, C.; Samuel, J. Controlled Phase Interactions Between Pulsed Electric Fields, Ultrasonic Motion, and Magnetic Fields in an Anodic Dissolution Cell. *J. Manuf. Sci. Eng.* **2018**, *140*, 041010. [CrossRef]
58. Tang, L.; Gan, W.M. Experiment and simulation study on concentrated magnetic field-assisted ECM S-03 special stainless steel complex cavity. *Int. J. Adv. Manuf. Technol.* **2014**, *72*, 685–692. [CrossRef]
59. Coey, J.M.D.; Hinds, G. Magnetoelectrolysis—The effect of magnetic fields in electrochemistry. In Proceedings of the 5th International Pamir Conference, Ramatuelle, France, 16–20 September 2002; pp. 1–7.
60. Qian, S.; Bau, H.H. Magneto-hydrodynamic stirrer for stationary and moving fluids. *Sens. Actuators B* **2005**, *106*, 859–870. [CrossRef]
61. Klocke, F.; König, W. *Fertigungsverfahren 3—Abtragen, Generieren und Lasermaterialbearbeitung*, 4th ed.; Springer: Berlin/Heidelberg, Germany, 2007.
62. Luther, F.; Schaarschmidt, I.; Schubert, A.; Richter, M. Strömungscharakterisierung im Arbeitsspalt beim magnetfeldüberlagerten elektrochemischen Abtragen. *Tech. Mess.* **2023**, *90*, 268–281. [CrossRef]
63. *FlowMaster: Product Manual for DaVis 10.2*; LaVision GmbH: Göttingen, Germany, 2021.